

UNIVERSITY OF CALIFORNIA, SAN DIEGO

Transport in Networks

A dissertation submitted in partial satisfaction of the
requirements for the degree
Doctor of Philosophy

in

Engineering Sciences (Engineering Physics)

by

Viktoría Rós Gísladóttir

Committee in charge:

Professor Daniel M. Tartakovsky, Chair
Professor Prabhakar Rao Bandaru
Professor Ratneshwar Lal
Professor Alison Lesley Marsden
Professor John Scott McCartney

2018

Copyright
Viktoría Rós Gísladóttir, 2018
All rights reserved.

The dissertation of Viktoría Rós Gísladóttir is approved, and it is acceptable in quality and form for publication on microfilm and electronically:

Chair

University of California, San Diego

2018

DEDICATION

To my family and friends, but most of all to Árni.

TABLE OF CONTENTS

| | | |
|--|--|------|
| Signature Page | | iii |
| Dedication | | iv |
| Table of Contents | | v |
| List of Figures | | vii |
| List of Tables | | ix |
| Acknowledgements | | x |
| Vita | | xii |
| Abstract of the Dissertation | | xiii |
| Chapter 1 | Introduction | 1 |
| | 1.1 Transport in Networks | 1 |
| | 1.2 Heat transport in fracture networks | 2 |
| | 1.3 Virus propagation through cyber networks and the system’s resilience | 6 |
| Chapter 2 | Particle methods for heat transfer in fractured media | 8 |
| | 2.1 Introduction | 8 |
| | 2.2 Problem formulation | 10 |
| | 2.2.1 Fracture networks models | 11 |
| | 2.2.2 Fluid flow in the network | 11 |
| | 2.2.3 Heat transfer in fracture-matrix systems | 12 |
| | 2.3 Particle method for heat transfer in fractured media | 13 |
| | 2.4 Simulations of heat transfer in geothermal reservoirs | 16 |
| | 2.4.1 Geothermal reservoir properties | 16 |
| | 2.4.2 Heat transfer simulations | 17 |
| | 2.5 Results and discussion | 19 |
| | 2.5.1 Anomalous heat transfer | 19 |
| | 2.5.2 Performance of geothermal systems | 21 |
| | 2.6 Conclusion | 22 |
| | Acknowledgements | 25 |
| Chapter 3 | Efficient simulations of heat transfer in fractured rocks | 35 |
| | 3.1 Introduction | 35 |
| | 3.2 Problem formulation | 37 |
| | 3.2.1 Fracture networks | 37 |

| | | | |
|----------------------------|-------|---|----|
| | 3.2.2 | Fluid flow and governing equations | 38 |
| | 3.2.3 | A particle-based algorithm for heat transfer | 39 |
| | 3.3 | Simulation set up | 41 |
| | 3.4 | Results and discussion | 44 |
| | 3.5 | Conclusion | 48 |
| Acknowledgements | | | 50 |
| Chapter 4 | | Lagrangian simulations of heat transfer in fractured rocks | 51 |
| | 4.1 | Introduction | 51 |
| | 4.2 | Problem Formulation | 54 |
| | 4.2.1 | Fracture Network represented by Sierpinski latices | 54 |
| | 4.2.2 | Heat transfer in fracture-matrix systems | 56 |
| | 4.3 | Particle method for heat transfer in fractured media with two dimensional diffusion in the matrix | 58 |
| | 4.3.1 | Probabilistic expression of temperature in single fractures | 58 |
| | 4.3.2 | Accounting for the presence of neighboring fractures | 59 |
| | 4.4 | Simulations | 66 |
| | 4.4.1 | Heat transfer simulations | 66 |
| | 4.5 | Results | 67 |
| | 4.5.1 | Comparison | 67 |
| | 4.5.2 | Heat transfer in fracture networks | 67 |
| | 4.6 | Conclusion | 70 |
| Acknowledgements | | | 71 |
| Chapter 5 | | Resilience of cyber systems with over- and under- regulation | 72 |
| | 5.1 | Introduction | 72 |
| | 5.2 | Model and example | 76 |
| | 5.2.1 | Employees susceptibility to the virus | 78 |
| | 5.2.2 | Infection propagating through the organization | 80 |
| | 5.2.3 | Resilience of the organization | 80 |
| | 5.3 | Results | 82 |
| | 5.4 | Conclusion | 82 |
| Acknowledgements | | | 85 |
| Chapter 6 | | Conclusions | 86 |
| | 6.1 | Heat transfer in fractured rocks | 86 |
| | 6.2 | Spread of viruses in cyber networks | 88 |
| | 6.3 | Future work | 89 |

LIST OF FIGURES

| | | |
|-------------|---|----|
| Figure 1.1: | A fracture network connecting two boreholes. The re-injection and the production borehole are on the left and right, respectively. | 3 |
| Figure 1.2: | The Performance of the system as a function of time for heat transport between two boreholes for Watanbe (W1, W2, W3) and Sierpinski (S1, S2, S3) networks. Thermal breakthrough for the Watanbe networks is around 10^8 and for Sierpinski Networks it is closer to 10^9 | 4 |
| Figure 2.1: | Fracture networks generated with the fracture network parameters presented in Table 2.1. The blue rectangles on the left and right sides of the domains represent the injection and extraction wells of the geothermal systems, respectively. | 26 |
| Figure 2.2: | Interconnected fracture networks related to the fracture networks presented in Fig. 2.1 and connecting the injection and extraction wells. | 27 |
| Figure 2.3: | Temporal variability of the relative temperature T^* in fracture network <i>DFN2a</i> with fractal dimension $D = 1$, for parameter sets (i)–(iv) in Table 2.2. | 28 |
| Figure 2.4: | Temporal variability of the relative temperature T^* in fracture networks <i>DFN1a</i> , <i>DFN2a</i> , and <i>DFN3a</i> (see Fig. 2.2), for the matrix properties from data set (ii) in Table 2.2 and (a) <i>Fast Flows</i> and (b) <i>Slow Flows</i> conditions. | 29 |
| Figure 2.5: | Temporal variability of the relative temperature \mathcal{T}^* in fracture networks <i>DFN1a</i> , <i>DFN2a</i> , and <i>DFN3a</i> (see Fig. 2.2), for the matrix properties from data set (ii) in Table 2.2 and (a) <i>Fast Flows</i> and (b) <i>Slow Flows</i> conditions. | 30 |
| Figure 2.6: | Temporal variability of the geothermal performance P_f of the fracture networks presented in Fig. 2.2 with the matrix properties from data set (ii) in Table 2.2, for the <i>Fast Flows</i> (left column) and <i>Slow Flows</i> (right column) conditions. | 34 |
| Figure 3.1: | Sierpinski networks with levels $M = 3$ (S1, left), $= 4$ (S2, center), and $= 5$ (S3, right). | 41 |
| Figure 3.2: | Top row: three Watanabe networks generated by equation (1) for the parameters in Table 3.2. Bottom row: backbones of these networks. | 42 |
| Figure 3.3: | The Performance of the system as a function of time for heat transport between two boreholes 100 m apart across fracture networks: S1, S2, and S3 (Figure 1) as well as W1, W2, and W3 (Figure 2) for Slow flow (left) and Fast flow (right) | 44 |
| Figure 3.4: | Temporal variability of the relative temperature of fracture networks (left) S1, S2, S3, (see Figure 1) and (right) W1, W2, and W3 (see Figure 2) for Fast flow hydraulic regime. | 46 |
| Figure 3.5: | The CPU for the varying fracture density for the Watanabe and Sierpinski Networks for Fast flow and Slow flow. | 46 |

| | | |
|-------------|--|----|
| Figure 3.6: | The temporal variation of the performance drop of the system over 100 m to levels of 80% and 50% for varying degrees of fracture density for Fast flow hydraulic regime. | 47 |
| Figure 4.1: | Sierpinski networks with levels 1, 2, and 3, respectively SL1, SL2, and SL3. | 56 |
| Figure 4.2: | Segmenting the fracture | 60 |
| Figure 4.3: | Three parallel fractures. The particles originate from the fracture at $y = 0$ and can diffuse to fractures located at $y = l_1$ or $y = l_2$ where they are absorbed. | 65 |
| Figure 4.4: | The temperature at the end of the fracture as a function of time computed with the analytical solution by Ruiz et. al 2012 treating the fracture as single segment (red solid line) and with the particle method and probabilistic generating functions where the fracture is made up of two segments (green circles). | 68 |
| Figure 4.5: | Sierpinski level 1,2, and 3 with one dimensional conduction in the matrix. | 69 |
| Figure 4.6: | Sierpinski level 1,2, and 3 with two dimensional conduction in the matrix. | 69 |
| Figure 5.1: | System risk is a function of the number of rules. The red line represents the risk from external threats; the blue line represents the risk from internal vulnerabilities; and the green line represents the combined risk from external threats and internal vulnerabilities. | 74 |
| Figure 5.2: | 1D users decision latitude model (9). | 78 |
| Figure 5.3: | Model of the business relationships network (a) and its nodes' minimum decision latitudes (b). Notably, users of higher degrees have a smaller value of the decision latitude, a higher number of strict barriers (red) and, hence, are less vulnerable [Magat et al., 1988]. | 79 |
| Figure 5.4: | a) Critical functionality of the system as a function of time for different numbers of rules, b) risk and c) resilience as functions of rules for different vulnerability levels. The shaded areas in panels b) and c) correspond to the values of risk and resilience for threat latitudes of 4.5 and 5.5 while the lines reflect the case of $L_T = 0.5$ | 83 |

LIST OF TABLES

| | | |
|------------|---|----|
| Table 2.1: | Parameters used to generate alternative fracture networks. | 31 |
| Table 2.2: | Physical properties of fractured rocks used to simulate heat transfer. | 32 |
| Table 2.3: | The Kolmogorov-Smirnov statistic S_{KS} for fracture networks characterized by their fractal dimension D and fracture density C | 33 |
| Table 3.1: | Global parameters for Sierpinski and Watanabe networks generation. | 43 |
| Table 3.2: | Network flow velocity values for Sierpinski and Watanabe networks for Slow and Fast flow. | 45 |
| Table 5.1: | Main acronyms, parameters, and variables of the model. | 76 |

ACKNOWLEDGEMENTS

I would like to thank and acknowledge my advisor Professor Daniel Tartakovsky for his guidance, mentoring, and support. My committee Professor Alison Marsden, Professor Prabhakar Bandaru, Professor Ratneshwar Lal, and Professor John McCartney for their time and support. Their mentoring, both technical and professional, helped build the path I took to make this thesis a reality.

I would like to thank Marjory Blumenthal, Ashley Predith, Diana Pankevich, DJ Patil and the rest of the people at Office of Science and Technology Policy as well as the PCAST members for broadening my horizon. It was a great experience to work with you and learn from you.

My gratitude goes out to my family and friends all over the world for their support. Special thanks go to David and Silvana who started this journey with me and stayed the course and my writing buddies Anne Therese and Tara. To the MAE nerds Ben, Francesca, Delphine, Negin, Ilenia, Matt, Cecily, and Alex. And all the other San Diego transplants that were along for the ride especially Berglind, Anna, Praveena, Kristín, Kaitlyn, the yoga community, and the Awesome San Diego crew. Katie thank you for everything. You truly are an inspiration and are missed. I would like to acknowledge the faith and support that I received from afar through all of it Hildur, Magga, Anna Karen, Tinna, Klara, Kolbrún, Thóra, Hrund, Hronn, Amma og Afi. Takk fyrir allt saman.

My deepest gratitude goes to my parents who always ensured that my curiosity had room to grow. My mother Sigga who made sure I had enough playing field for my mind. My father Gísli who encouraged me to live a life of the mind and showed me how to enjoy it. His continued faith in me has been such a source of strength.

Most of all my gratitude goes to my husband Árni. For his support, patience, and love. It has been a pleasure to have you with me on this journey my love.

The text of this dissertation contains reprints of the following papers, either accepted or submitted for consideration at the time of publication. The dissertation author was the primary investigator and author of these publications.

Chapter 2

Gisladottir, V., Roubinet D., Tartakovsky D., “Particle methods for heat transfer in fractured rocks”, *Transport in Porous Media*, 115:311-326. 2016.

Chapter 3

Gisladottir, V., Roubinet D., Tartakovsky D., “Efficient simulations of heat transfer in fractured rocks”, *PROCEEDINGS, 43rd Workshop on Geothermal Reservoir Engineering*. 2018.

Chapter 4

Gisladottir, V., Roubinet D., Tartakovsky D., “Lagrangian simulations of heat transfer in fractured rocks”, (in preparation for submission)

Chapter 5

Gisladottir, V., Ganin A., Keisler J., Kepner J., Linkov I., “Resilience of Cyber Systems with Over-and Under-regulation”, *Risk Analysis*. 37.9:1644-1651. 2016

VITA

- 2008 B. S. in Mechanical Engineering first class, University of Iceland
- 2011-2014 Graduate Teaching Assistant, University of California, San Diego
- 2012 M. S. in Engineering Science (Mechanical Engineering), University of California, San Diego
- 2018 Ph. D. in Engineering Science (Engineering Physics), University of California, San Diego

PUBLICATIONS

Gisladottir, V., Roubinet D., Tartakovsky D., “Lagrangian simulations of heat transfer in fractured rocks”, (in preparation for submission).

Gisladottir, V., Roubinet D., Tartakovsky D., “Efficient simulations of heat transfer in fractured rocks”, PROCEEDINGS, 43rd Workshop on Geothermal Reservoir Engineering, 2018.

Seager, T., Gisladottir V., Mancillas J., Roege P., Linkov I., “Inspiration to Operation: Securing Net Benefits vs. Zero Outcome”, Journal of Cleaner Production, 2017

Gisladottir, V., Roubinet D., Tartakovsky D., “Particle methods for heat transfer in fractured rocks”, Transport in Porous Media, 2016.

Gisladottir, V., Ganin A., Keisler J., Kepner J., Linkov I., “Resilience of Cyber Systems with Over- and Underregulation”, Risk Analysis , 1644-1651, 2016

Linkov, I., Gisladottir, V., Wood, M., “Decision Making in a Convergent Society”, Handbook of Science and Technology Convergence Ed. M. Roco Springer, 2015

Hjartarsson, G., Gisladottir, V., Gislason G., “Geothermal Development in the Assal Area, Djibouti”, Proceedings of the World Geothermal Congress International Geothermal Association, 2010

ABSTRACT OF THE DISSERTATION

Transport in Networks

by

Viktoría Rós Gísladóttir

Doctor of Philosophy in Engineering Sciences (Engineering Physics)

University of California, San Diego, 2018

Professor Daniel M. Tartakovsky, Chair

Transport in networks represents a class of important phenomena that occur in many natural and anthropogenic settings. This dissertation deals with two such processes: heat transport in fracture networks in the subsurface and resiliency response of a cyber network to virus propagation. Numerical simulations of heat transfer provide insight into the performance of subsurface systems (e.g. geothermal reservoirs) and the potential for their enhancement. Standard, grid-based method of heat transfer are computationally expensive, often prohibitively so [Karra et al., 2018], due to a vast discrepancy of scales between fracture apertures (millimeter scale) and the ambient rock matrix domain (meter scale). In Chapter 2, we present a mesh-free time-domain particle method for modeling heat transfer in highly heterogeneous fractured media.

Our method is orders of magnitude faster than its grid-based alternatives and is readily adaptable to different network configurations. We deploy this method to model heat extraction from geothermal reservoirs by using a fractal network representing faults and damage zones. Our analysis reveals anomalous behavior of heat transfer in fractured environments due to existence of preferential flow paths. It also demonstrates a significant impact of the networks topology on the performance of geothermal reservoirs. In Chapter 3, this method is used to investigate the impact of fracture network properties on geothermal performance. Specifically, we explore how fracture-network topology and matrix-block size distribution control, respectively, the advective and conductive mechanisms of heat transfer in fractures and ambient matrix, as well as the heat flux exchanged between these structures. To accomplish this goal, we examine two different conceptual descriptors of fracture networks over a variety of hydraulic conditions and fracture-generating parameters, and the effects of topologic properties and hydraulic conditions on computational time. In Chapter 4 we further generalize our mesh-free particle method by removing the physical assumption of one-dimensional conduction in the matrix. This is achieved by accounting for both longitudinal and transversal heat conduction in the matrix. It looks at the impact of removing set assumption and identifies the parameter set where it is of importance. Finally, in Chapter 5, we explore transport in anthropogenic networks by presenting a method to simulate the resiliency response of a cyber network to a virus propagation. We identify the need for systematic data collection and appropriate metrics to enable data driven optimization of the rule base. As well as demonstrate that the optimal number of rules necessary to regulate a cyber network efficiently is likely to be small and focused on specific critical functions that the system needs to maintain.

Chapter 1

Introduction

1.1 Transport in Networks

As we move through the world, we encounter networks everywhere – both natural and anthropogenic. Examples in the natural world include large-scale rock formations and river networks. On a smaller scale, there are neural-networks and biological networks. Anthropogenic networks likewise take many forms. Whether they are telecommunication networks, which enable us to interact with the world through phone, cable, and the Internet, or transportation networks, which take the form of highways, railways and roads, anthropogenic networks are something that we use everyday.

All of the previously mentioned networks have one thing in common: transport takes place in all of them. The form of dynamics and the items being circulated might change, transportation remains constant. In rock formations, fluid, solute, and heat are transported across the networks. Rivers transport all of these natural physical phenomena as well as boats, wildlife, trash, and pollution. Neural networks facilitate neuron transport as biological systems interact with each other in the form of networks exchanging information [Truskey et al., 2004]. These communication networks route messages across data networks [Schwartz and Stern, 1980], while

highways, railroads and roads transport vehicles and commodities [Barthélemy, 2011, Boeing, 2017].

1.2 Heat transport in fracture networks

The ground we stand on feels so familiar, but do we really know it or its potential? Underneath the surface lies a fractured porous medium that can work as heat, oil, nuclear, or even solute storage with preferential pathways, in the form of fluid flow in fractures. Modeling capabilities of these processes, including heat transfer, have been used to leverage reservoirs potential. Models of heat transfer in a fractured medium are used to optimize the performance of geothermal energy harvesting [Saar, 2011] and secondary (enhanced) oil recovery [Al-Hadhrami and Blunt, 2001], to interpret tests that use anthropogenically generated [Wagner et al., 2014] heat as a groundwater tracer; and to optimize the design of building's cooling/heating installations via ground heat exchangers [Ciriello et al., 2015]. Modeling is additionally used to assist with mitigating the potential negative environmental impact of subsurface heat generation due to, e.g., radioactive decay from a nuclear waste leakage [Wang et al., 1981] or creation and/or reopening of microfractures from geothermal energy harvesting [Chen and Shearer, 2011].

Geothermal energy is useful for district heating and electricity generation. While countries such as New Zealand and Iceland use it as their primary energy source, the United States does not. Yet, the United States could fulfill about 20% of its energy needs with geothermal energy using current technology [DOE, 2015]. Geothermal energy production relies on the heat from the subsurface to fuel steam turbines to produce electricity or to heat water for district heating and domestic use. A geothermal reservoir has to have three components for harvesting to be feasible: heat, fluid and fractures. The harvesting process requires extracting geothermal fluid from a reservoir through boreholes. The heat from the fluid is then extracted for energy production. After the heat has been extracted, the fluid is re-injected into the reservoir to preserve

the pressure of the system, which is critical to maintaining the sustainability and therefore the production of the reservoir. This step of re-injection is also critical to minimizing environmental impact by preventing the formations of geothermal fluid lagoons. Although the re-injection boreholes are vital, they run the risk of introducing cooler fluid to a production site and thus causing performance to drop at a production site. Designing the layout of boreholes determines the economic feasibility of a given energy production site. To optimize the energy production it is critical to locate production boreholes at resource rich locations and to locate re-injection boreholes at sites where they will have minimal impact on neighboring production sites. Understanding the heat transfer across the fractured media connecting the boreholes is essential to optimize this interaction. Figure 1.1 shows re-injection and production boreholes and the fracture networks connecting them.

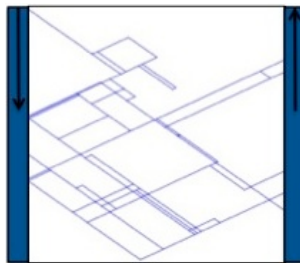


Figure 1.1: A fracture network connecting two boreholes. The re-injection and the production borehole are on the left and right, respectively.

This thesis focuses on modeling heat transfer across such networks to show the thermal breakthrough and gradient at a production site, which indicates the performance of a system (e.g. reservoir). The longer it takes for a thermal breakthrough and the flatter the gradient, the higher the performance of the system will be (see Figure 1.2).

Scenarios where there are opportunities to optimize the engineering of a reservoir based on heat transfer models include characterization of the percolation at potential sites during feasibility studies, and estimation of the environmental impact of using them as a waste storage site or industrial site. For that purpose anthropogenic heat can be used as a ground tracer [Molson

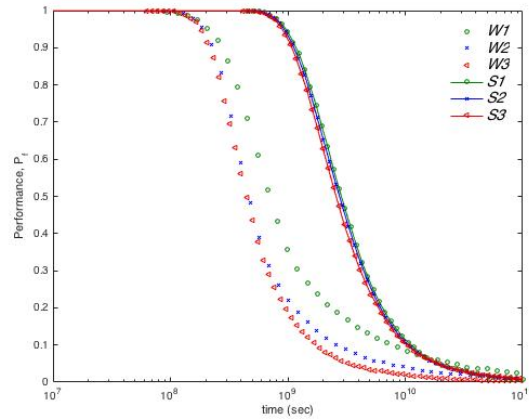


Figure 1.2: The Performance of the system as a function of time for heat transport between two boreholes for Watanbe (W1, W2, W3) and Sierpinski (S1, S2, S3) networks. Thermal breakthrough for the Watanbe networks is around 10^8 and for Sierpinski Networks it is closer to 10^9 .

et al., 2007]. Additionally, the models are useful for hot field geothermal energy harvesting where the network's topology determines the geothermal performance via its influence on preferential flow paths and the spatial extent of the heat extraction area and therefore the heat flux exchange between the fractures and the surrounding matrix. The former can be altered with reservoir stimulation techniques (e.g. hydraulic fracturing), and the latter by changing hydraulic conditions (e.g. flow rates). Numerical simulations of heat transfer in fractured media aid with analysis, design, and implementation of set sites. Because of the many different benefits of having reservoir models and all the challenges of applying them effectively, many different types of modeling techniques have been developed.

As one pursues the goal of capturing the transport processes in a model, approximations have to be made. All models are an idealized approximation of reality and none are truly correct. The challenges involved in modeling heat transfer in fractured medium are due to the scale separation between the fracture aperture (millimeter scale) and the fracture length/matrix size (meter scale), in addition to the stark contrast of the hydraulic and thermal properties between the fluid-filled fractures and the rock matrix [Bonnet et al., 2001, de Dreuzy et al., 2001a,b].

This complex nature requires models to balance computational efficiency with simplifications of geometric features of the fracture networks and physical transport processes (e.g. dimensions). Two common descriptors of a fractured medium, discrete fracture networks (DFN) and continuum models, address these challenges in different ways. The DFN descriptor has the advantage of being able to capture preferential flow paths, but it is usually paired with grid-based heat transfer methods, which can get very resource-intensive due to the scale separation. While continuum models do not have the same resource constraint, they do not necessarily capture the anomalous (non-Fourrierian) behavior of heat transfer that appears due to preferential flow paths. The specific focus of the heat transfer part of this dissertation is to address these challenges by using discrete fracture networks as a descriptor for a novel particle-based heat transfer model that captures preferential flow pathways and does not require the resource intensity of a grid-based method. This model is then used to examine the reservoir's response which can inform the engineering of the system.

In Chapter 2, the particle method for heat transfer in fracture networks is presented. We study the impact of fracture-network topology and hydraulic regimes on heat transfer by performing simulations for a range of fracture-network properties and experimental conditions. Numerical experiments are done simulating the heat transfer across a Watanabe network connecting an injection and production borehole at a geothermal site, as the Watanabe networks are characteristic of geothermal reservoirs. We look at the thermal breakthrough, i.e. the potential of the fluid from the injection site cooling down the production site. Our results demonstrate a significant impact of the network topology on the performance of geothermal reservoirs. Additionally, they demonstrate anomalous behavior of heat transfer in fractured environments.

In Chapter 3, we apply the method from Chapter 2 to two different conceptual descriptors of fracture networks, Sierpinski and Watanabe, a range of hydraulic conditions, and a range of fracture-generating parameters. This allows for the exploration of fracture-network topology and matrix-block size distribution control of the advective mechanism in the fractures and the

conductive mechanisms in the matrix, as well as the heat flux exchange between the two. We also look at the topologies' properties and hydraulic conditions impact on the CPU efficiency of the simulations. Our results demonstrate that for some hydraulic regimes, the performance of the two network descriptors can differ by close to an order of magnitude, while in others the difference is not as stark although still present. Another finding is that the CPU efficiency is sensitive to the hydraulic properties to some extent but is not greatly affected by topological properties.

The particle model used in Chapter 2 and 3 relies on the assumption of one-dimensional conduction in the matrix. In Chapter 4, we present a particle method that extends that model to include multi-dimensional conduction in the matrix. Numerical experiments are performed on Sierpinski networks to study the effects of fracture-network topology and matrix-block size distribution control, respectively, the advective and conductive mechanisms of heat transfer in fractures and ambient matrix as well as the heat flux exchanged between these structures. Additionally we look at the effects of the multi-dimensional versus one-dimensional conduction in the matrix.

1.3 Virus propagation through cyber networks and the system's resilience

Cyber vulnerability is an increasing threat to critical systems and infrastructure. A common reaction to a new threat or vulnerability is to add new rules that users have to follow. However, it is unclear if more rules enhance overall system resilience. Evidence to the contrary exists. Resilience is the ability of a system to absorb, recover, and adapt to known and unknown threats.

In Chapter 5 we present a framework that models a relationship between number of rules that users must follow and resilience of an organization. We identify the need for systematic

data collection and appropriate metrics to enable data driven optimization of the rule base. For this purpose, we have a network with a scale-free configuration model, which takes into account the heavy-tail degree distribution often found in communication systems. At each node, there is an employee with decision latitude. The decision latitude directly impacts the vulnerability and the resilience of the network. We argue that while increasing the number of rules may decrease direct threats from external attacks, the excessive regulations actually increase internal vulnerabilities due to the unintentional violations of operational rules by insiders. Therefore, the optimal number of rules necessary to regulate a cyber network efficiently is likely to be small and focused on specific critical functions that the system needs to maintain.

Chapter 2

Particle methods for heat transfer in fractured media

2.1 Introduction

Mathematical modeling of heat transfer in subsurface environments plays an important role in many fields of science and engineering. It has been used to optimize the performance of enhanced oil recovery by reducing oil viscosity with the injection of hot water or steam [Al-Hadhrami and Blunt, 2001] and ground heat exchangers used in cooling/heating of buildings [Ciriello et al., 2015], and to characterize subsurface environment by treating geothermal [Saar, 2011] and anthropogenically generated [Wagner et al., 2014] heat as a groundwater tracer. It has also been deployed to forecast the adverse affects of subsurface heat generation and transfer, such as creation and/or reopening of microfractures leading to seismic activity induced by geothermal energy extraction [Chen and Shearer, 2011] and nuclear waste leakage due to heat generated by radioactive decay [Wang et al., 1981].

In geothermal reservoirs, advection is the dominant mechanism of heat transfer within a fracture network, while the ambient matrix acts as the principal heat-storage medium [Bruehl, 2002,

Kolditz, 1995, Ruiz Martinez et al., 2014]. A network's topology determines the spatial extent of a heat extraction area, and the heat flux exchanged between fractures and the surrounding matrix controls the geothermal performance. The former can be modified with reservoir stimulation techniques (e.g., hydraulic fracturing), and the latter can be affected by varying hydraulic conditions (e.g., flow rates). Numerical models of heat transfer in fractured media facilitate design and implementation of both strategies.

These models must contend with a strong contrast in the hydraulic and thermal properties of fluid-filled fractures and the surrounding rock matrix, as well as with heterogeneous fracture networks that span a hierarchy of scales and often exhibit fractal behavior [Bonnet et al., 2001, de Dreuzy et al., 2001a,b]. Such fractured media might not have a representative elementary volume. Hence, they are not amenable to standard homogenization [Long et al., 1982, Painter and Cvetkovic, 2005, Roubinet et al., 2010a] and modeling based on a single-continuum advection-dispersion equation (ADE). Two conceptual frameworks have been proposed to tackle this problem in the context of solute transport. The first treats a fractured rock as a stochastic continuum, whose transport properties are random fields; one postulates either the existence of a scale on which the (stochastic) ADE is valid [Neuman, 2005] or the absence of such a scale by adopting instead, e.g., continuous time random walk (CTRW) models [Berkowitz and Scher, 1997]. Both approaches predict anomalous (non-Fourier-like) average behavior of solute transport in fractured media [Scher et al., 2002, Neuman and Tartakovsky, 2009, Cushman et al., 2011]. CTRW has also been used to model the anomalous behavior of heat transfer in heterogeneous and fractured media [Emmanuel and Berkowitz, 2007, Geiger and Emmanuel, 2010].

The second modeling framework explicitly incorporates dominant fractures into mathematical representations of the subsurface, i.e., replaces the continuum-medium representation of fractured rocks with two non-overlapping continua: a fluid-filled discrete fracture network (DFN) and the ambient rock matrix. Mass transfer models of this sort have been applied to

both deterministic [Dverstorp et al., 1992, Nordqvist et al., 1992] and stochastic [Cacas et al., 1990, Ezzedine, 2010] fracture networks. Numerical solutions of such models must combine a meter-scale discretization of the matrix with a millimeter-scale discretization of fracture apertures, which makes them computationally intensive, often prohibitively so. This has led to the development of mesh-free, particle-based solvers for solute transport in fractured rocks [Painter et al., 2008, Roubinet et al., 2010b]. We are not aware of similar methods for heat transfer.

To study heat transfer due to injection of fluids into fractured geothermal reservoirs, we adopt the particle-based method of [Roubinet et al., 2010b]. The computational efficiency of this method allows us to handle site-specific fractal geometries of fracture networks characteristic of geothermal reservoirs and the hydraulic conditions representative of geothermal systems. Our simulations, conducted on a wide range of fracture network parameters and experimental conditions, reveal the anomalous behavior of heat transfer in heterogeneous fractured media. They also demonstrate the significant impact of the network properties and hydraulic conditions on the performance of geothermal reservoirs. Section 2.2 contains a description of the fracture network and heat transfer models used in our analysis. In Section 2.3 we describe the mesh-free numerical method used to solve this problem, and present a set of numerical experiments in Section 2.4. The simulations results are interpreted and discussed in Section 4.5.

2.2 Problem formulation

To study geothermal energy harvesting, we consider fracture networks that are representative of geothermal reservoirs. The fracture network construction is described in Section 2.2.1, and models of fluid flow and heat transfer on these networks are formulated in Sections 2.2.2 and Sections 2.2.3, respectively.

2.2.1 Fracture networks models

Following [Watanabe and Takahashi, 1995], we consider a fractal fracture network model of geothermal reservoirs. The model defines the number of fractures N_f and the length r_i of the i th fracture ($i = 1, \dots, N_f$) as

$$N_f = \text{int}(C/r_0^D), \quad r_i = (C/i)^{1/D}, \quad (2.1)$$

where the function $\text{int}(x)$ rounds x up to the next integer and D is the fractal dimension (a fitting parameter). The remaining two parameters, the fracture density C and the smallest fracture length r_0 , can be estimated from a core sample. The fracture network is constructed by treating the midpoint of each fracture pair as a random variable. The angle between the pair of fractures can take one of the two prescribed values, θ_1 or θ_2 , with equal probability. The fracture's aperture b is constant and the same for all fractures.

2.2.2 Fluid flow in the network

We consider steady-state laminar flow of an incompressible fluid, which takes place in the fracture network while treating the ambient rock matrix as impervious. Assuming that a fracture is formed by two parallel smooth plates and that the fluid density ρ and dynamic viscosity μ remain constant, the Poiseuille law results in the average flow velocity u given by

$$u = -\frac{\rho g b^2}{12\mu} J. \quad (2.2)$$

Here g is the gravitational acceleration constant, and J is the hydraulic head gradient along the fracture. Enforcing mass conservation at fracture junctions and applying expression (2.2) to each fracture segment leads to a linear system $\mathbf{A}\mathbf{h} = \mathbf{b}$ where \mathbf{h} is the vector of the (unknown) hydraulic heads at fracture junctions [e.g., Long et al., 1982, de Dreuzy et al., 2001a]. Given the

global pressure gradient imposed on the outer edges of the network, we solve this linear system and use the resulting hydraulic heads to compute the average flow velocity in each fracture of the network.

2.2.3 Heat transfer in fracture-matrix systems

The particle method described in Section 2.3 constructs a solution to the problem of heat transfer in fracture networks from a solution to the problem of heat transfer in an individual fracture, with aperture b and semi-infinite length, embedded in an infinite matrix. The latter problem is formulated as follows. The fracture is represented by $\Omega_f = \{(x, z) : 0 \leq x < \infty, |z| \leq b/2\}$ and the matrix by $\Omega_m = \{(x, z) : 0 \leq x < \infty, |z| \geq b/2\}$. Fluid temperature in the fracture, $T^f(x, z, t)$, satisfies an advection-dispersion equation (ADE)

$$\frac{\partial T^f}{\partial t} + u \frac{\partial T^f}{\partial x} = D_L^f \frac{\partial^2 T^f}{\partial x^2} + D_T^f \frac{\partial^2 T^f}{\partial z^2}, \quad (x, z) \in \Omega_f, \quad (2.3)$$

where u is the fluid velocity computed in Section 2.2.2, and D_L^f and D_T^f are the longitudinal and transverse dispersion coefficients, respectively. These coefficients are defined as $D_L^f = \lambda_L^f / (\rho c) + E_L^f / (\rho c)$ and $D_T^f = \lambda_T^f / (\rho c) + E_T^f / (\rho c)$, where c is the fluid's heat capacity; λ_L^f and λ_T^f are the longitudinal and transverse thermal conductivity coefficients, respectively; and E_L^f and E_T^f are the longitudinal and transverse thermal dispersion coefficients, respectively [Yang and Yeh, 2009].

Since the ambient matrix Ω_m is assumed to be impervious to flow, temperature in the matrix, $T^m(x, z, t)$, is governed by a diffusion equation (DE)

$$\frac{\partial T^m}{\partial t} = D_L^m \frac{\partial^2 T^m}{\partial x^2} + D_T^m \frac{\partial^2 T^m}{\partial z^2}, \quad (x, z) \in \Omega_m, \quad (2.4)$$

where D_L^m and D_T^m are the longitudinal and transverse diffusion coefficients, respectively. These

coefficients are defined as $D_L^m = \lambda_L^e/c_e$ and $D_T^m = \lambda_T^e/c_e$, where c_e is the effective heat capacity of the matrix; and λ_L^e and λ_T^e are the longitudinal and transverse thermal conductivity coefficients in the matrix, respectively.

At the fracture-matrix interfaces $|z| = b/2$, the continuity of both temperature and heat flux is enforced with conditions

$$T^f = T^m, \quad \phi_m D_T^m \frac{\partial T^m}{\partial z} = D_T^f \frac{\partial T^f}{\partial z}, \quad |z| = b/2, \quad (2.5)$$

where $\phi_m = [\phi + (1 - \phi)\rho_s c_s / (\rho c)]$; ϕ is the matrix porosity; and ρ_s and c_s are the density and heat capacity of the solid phase, respectively. Finally, equations (4.1) and (4.2) are subject to initial conditions

$$T^f(x, z, 0) = T_0, \quad T^m(x, z, 0) = T_0, \quad (2.6)$$

and boundary conditions

$$T^f(0, z, t) = T_{inj}, \quad T^f(+\infty, z, t) = T_0, \quad T^m(x, \pm\infty, t) = T_0, \quad (2.7)$$

where $T_0(x, z)$ is the initial temperature in the system, and T_{inj} the temperature of the fluid injected at the entrance of the fracture.

Since the heat transfer problem (4.1)-(4.5) is invariant under transformations $T = T^i - T_0$ ($i = f, m$), we set, without loss of generality, $T_0 = 0$.

2.3 Particle method for heat transfer in fractured media

Since the underlying mathematical structure of the heat and mass transfer problems is the same, we adapt the particle method of [Roubinet et al., 2010b], which was developed to

model solute transport, to describe heat transfer in fractured rocks. The method consists of three parts: i) at the fracture-matrix scale, heat transfer is described by advection in the fracture and conduction in the infinite matrix; ii) at the matrix-block scale, heat conduction in the matrix is restricted by the presence of neighboring fractures, into which particles can transfer; and iii) at the fracture-network scale, heat flux conservation is enforced at each fracture intersection by considering that the probability for a particle to enter a fracture depends on the intersection configuration and flow rate distribution.

At the fracture-matrix scale, we use the analytical solution of [Tang et al., 1981], which is derived under the following simplifications of the boundary-value problem (4.1)–(4.5). First, the ADE (4.1) is averaged over the fracture aperture to replace it with its one-dimensional counterpart. Second, longitudinal dispersion in the fracture is assumed to be negligible relative to convection. Third, diffusion in the matrix is assumed to be one-dimensional, in the direction perpendicular to the fracture. Finally, the flux continuity expressed by the second condition in (2.5) at the fracture-matrix interfaces is replaced by a source term in the fracture equation, which depends only on the matrix properties. Under these conditions, whose validity has been studied by [Roubinet et al., 2012], the temperature distribution inside the fracture is given by

$$T^f(x, t) = T_{\text{inj}} \operatorname{erfc} \left(\frac{\phi_m \sqrt{D_T^m} x}{2ub \sqrt{t - x/u}} \right). \quad (2.8)$$

This expression is converted into a probabilistic model for a particle's diffusion time in infinite matrix, t_d^∞ , as

$$t_d^\infty = \left[\frac{\phi_m \sqrt{D_T^m} t_a}{2b \operatorname{erfc}^{-1}(R)} \right]^2, \quad t_a = \frac{x}{u} \quad (2.9)$$

where R is a uniform random number in the interval $[0, 1]$, and t_a is the advection time spent in the fracture to reach the position x .

To take into account the impact of potential neighboring fractures (i.e., the finite size of matrix blocks), we consider the scenario of a fracture f_i surrounded by i) a fracture f_1 located at

distance l_1 on one side of f_i , and ii) a fracture f_2 located at distance l_2 on the other side of f_i . For each particle that diffuses into the matrix surrounding f_i , we define P_{transfer}^1 as the probability to reach fracture f_1 without crossing fracture f_2 , and P_{transfer}^2 as the probability to reach fracture f_2 without crossing fracture f_1 . These probabilities in the Laplace domain are given by [Feller, 1954]

$$\bar{P}_{\text{transfer}}^1 = \frac{\exp(l_1 \sqrt{s/D_T^m})}{s} \frac{1 - \exp(-2l_2 \sqrt{s/D_T^m})}{1 - \exp[2(l_1 - l_2) \sqrt{s/D_T^m}]} \quad (2.10a)$$

$$\bar{P}_{\text{transfer}}^2 = \frac{\exp(l_2 \sqrt{s/D_T^m})}{s} \frac{1 - \exp(-2l_1 \sqrt{s/D_T^m})}{1 - \exp[2(l_2 - l_1) \sqrt{s/D_T^m}]}, \quad (2.10b)$$

where s is the Laplace variable. The numerical inversion of these expressions is performed with the [Stehfest, 1970] algorithm. The final diffusion time of each particle and its final position after diffusing in the matrix are computed in two steps. First, we determine P_{transfer} , the probability for a particle to transfer to one of the neighboring fractures with an associated transfer time t_{transfer} smaller than the maximum diffusion time t_d^∞ , as

$$P_{\text{transfer}} = P_{\text{transfer}}^1(t_{\text{transfer}} \leq t_d^\infty) + P_{\text{transfer}}^2(t_{\text{transfer}} \leq t_d^\infty). \quad (2.11)$$

Second, we pick a random number U from a uniform distribution on the interval $[0, 1]$: if U is larger than P_{transfer} , the particle does not transfer to the neighboring fractures (i.e., the particle goes back to its initial fracture) and its diffusion time is equal to t_d^∞ (i.e., the assumption of infinite matrix is valid); otherwise, the particle transfers to one of the neighboring fractures, the transfer time is defined by solving $P_{\text{transfer}}(t \leq t_{\text{transfer}}) = U$, and the particle transfers to fracture

f_1 if condition

$$\frac{U}{U_{\max}} > \frac{l_1}{l_1 + l_2} \quad (2.12)$$

is verified and to f_2 otherwise with $U_{\max} = P_{\text{transfer}}$. This method enables us to handle the presence of neighboring fractures in heterogeneous fracture networks. In the context of solute transport, a comparison between this approach and analytical solutions considering either a single fracture [Tang et al., 1981] or infinite systems of parallel fractures [Sudicky and Frind, 1982] is provided in [Roubinet et al., 2010b, 2013b].

Finally, when a particle reaches a fracture intersection that forks into multiple fractures, which fracture it transitions into is determined based on the intersection configuration and flow rate distribution. The particles can only enter into fractures that have a positive flow velocity (i.e., a fluid flowing from the studied intersection to another intersection) considering complete mixing and streamline routing rules [Hull and Koslow, 1986, Berkowitz et al., 1994]. In most cases, complete mixing is assumed and the probability for a particle to enter into a fracture is expressed as the ratio of the flow rate in the considered fracture to the sum of the flow rates leaving the studied intersection. A particular case is considered when a particle can enter into two fractures: if the closest fracture has a dominant flow rate, the particle goes in priority to this fracture [Le Goc, 2009a].

2.4 Simulations of heat transfer in geothermal reservoirs

2.4.1 Geothermal reservoir properties

To study heat transfer in realistic geothermal reservoir models, we consider a square domain of length $L = 100$ m, whose left and right borders are connected by a fracture network. The latter has the fractal dimension $D = [1, 1.3]$ which has been observed in the natural environ-

ments [Main et al., 1990, Scholz et al., 1993], and fracture density $C = [2.5, 6.5]$ [Watanabe and Takahashi, 1995]. Three groups of fracture networks, $DFN1$, $DFN2$ and $DFN3$, are defined with a fracture density set to $C = 2.5, 4.5$ and 6.5 , respectively. For each group, we generate four fracture networks with a fractal dimension set to $D = 1, 1.1, 1.2$ and 1.3 . Table 2.1 shows the parameters used to generate these fracture networks which are presented in Fig. 2.1.

Injection and extraction of fluid in these domains are simulated by considering injection and extraction wells located on the left and right borders of the domains, respectively. Two hydraulic regimes are applied between these wells in order to study different conditions of the geothermal exploitation. To this end, we define the *Fast Flows* regime where the head gradient is equal to 1.25 MPa as considered in existing studies on geothermal systems [Suzuki et al., 2015]. For comparison, we also define the *Slow Flows* regime where the head gradient is set to 10^{-2} MPa. Considering a no-flow condition on the bottom and top borders of the domain, a flow going from the left to right borders of the domains is observed through the interconnected fracture networks. The corresponding flow velocity fields are computed with the fluid density $\rho = 10^3 \text{ kg/m}^3$ and the dynamic viscosity $\mu = 10^{-3} \text{ kg/(m}\cdot\text{s)}$, on the interconnected fracture networks shown in Fig. 2.2.

2.4.2 Heat transfer simulations

Heat transfer is simulated in the interconnected fracture networks presented in Fig. 2.2 assuming an infinite matrix around each domain. For each fracture network and each flow regime, particles are injected into the fractures that intersect the injection well (left border of the domain), they are transported across the domain according to the heat transfer particle method presented in Section 2.3, and their arrival time to the production borehole (right border of the domain) is recorded. The rock porosity is $\phi = 0.1$ and the thermal parameters are provided in Table 2.2. These form data set (i) from [Lippmann and Bödvarsson, 1983], data set (ii) from [Pruess et al., 1999], data set (iii) from [Bödvarsson and Tsang, 1982], and data set (iv) from [Geiger

and Emmanuel, 2010].

Figure 2.3 exhibits the relative temperatures in the fracture network *DFN2a* with *Fast Flow* (Fig. 2.3a) and *Slow Flow* (Fig. 2.3b), for the thermal parameters representative of the values found in geothermal fields (Table 2.2). The between-set variability is not significant and has only minor impact on the temperature curves. Therefore, in the simulations presented below we use the parameter set (ii) in Table 2.2.

Figure 2.4 shows the corresponding relative temperature curves for the interconnected fracture networks *DFN1a*, *DFN2a* and *DFN3a* and the *Fast Flows* (Fig. 2.4a) and *Slow Flows* (Fig. 2.4b) regimes. In these figures, the relative temperature T^* is defined as

$$T^* = \frac{T_{\text{ext}} - T_0}{T_{\text{inj}} - T_0} \quad (2.13)$$

with T_{ext} the temperature of the fluid extracted at the right extremity of the domain for a continuous injection, at the left extremity of the domain, of a fluid at temperature T_{inj} . These curves are obtained from the cumulative distribution functions (CDFs) of the particle arrival times using $N = 1855$ particles, and these results are similar to those obtained from 10^4 particles.

This empirical CDF $T^*(t)$ deviates significantly from the Gaussian CDF $\mathcal{G}(t)$, with the same mean \bar{t} and standard deviation σ_t , over wide ranges of the fractal dimension D and fracture density C . This finding is reported in Table 2.3 in terms of the Kolmogorov-Smirnov (KS) statistic [Lurie et al., 2011] [Chapter 11.8]

$$\mathcal{S}_{\text{KS}} \equiv \max_{1 \leq i \leq N} |\mathcal{G}(t_i) - T^*(t_i)| = \max_{1 \leq i \leq N} \left\{ \left| \mathcal{G}(t_{i-1}) - \frac{i-1}{N} \right|, \left| \frac{i}{N} - \mathcal{G}(t_i) \right| \right\} \quad (2.14)$$

where $\{t_1, \dots, t_N\}$ are the particle arrival times arranged in the ascending order. The KS goodness-of-the-fit test rules out the hypothesis that the CDF $T^*(t)$ is Gaussian and, hence, that heat transfer in fractured rocks follows Fourier's law, with any degree of confidence. For example, the 5% (or 20%) level of significance requires \mathcal{S}_{KS} not to exceed the critical value $\mathcal{S}_{\text{KS}}^* \approx 1.36/\sqrt{N} = 0.0316$

(or $\approx 1.07/\sqrt{N} = 0.0248$ [Lurie et al., 2011, Table T-13], but the values of S_{KS} in Table 2.3 are more than an order of magnitude larger than S_{KS}^* . Even with the caveat that the mean \bar{t} and variance σ_t^2 of the Gaussian CDF $\mathcal{G}(t)$ should ideally be determined from simulations of an effective model rather than N samples, the discrepancy between S_{KS} and S_{KS}^* is so large as to demonstrate the anomalous (non Fourier-like) nature of heat transfer in fractured rocks.

To elucidate this anomalous behavior further, we define a relative temperature T^* , which corresponds to the relative temperature T^* for an instantaneous temperature change of the injected fluid. Figure 2.5 shows the temperature distribution in the interconnected fracture networks *DFN1a*, *DFN2a* and *DFN3a* for the *Fast Flows* (Fig. 2.5a) and *Slow Flows* (Fig. 2.5b) hydraulic configurations. These results are obtained by transforming the CDFs presented in Fig. 2.4 into the probability density functions (PDFs). Here 10^6 particles have been used in order to obtain smooth curves, and these results are similar to those obtained with 10^7 particles.

Geothermal performance of fractured reservoirs is often reported in terms of $P_f = 1 - T^*$, such that $P_f = 0$ represents the minimum efficiency of the system as the temperature of the extracted fluid is equal to the temperature of the (here cooler) injected fluid. Conversely, $P_f = 1$ represents the maximum efficiency of the system as the temperature of the extracted fluid is equal to the (here warmer) initial temperature of the system. Figure 2.6 shows the temporal profiles $P_f(t)$ for all considered fracture networks and for both the *Fast Flows* and *Slow Flows* hydraulic regimes. As in Fig. 2.4, these results are obtained using 10^3 particles and they are similar to those obtained from 10^4 particles.

2.5 Results and discussion

2.5.1 Anomalous heat transfer

The results presented in Fig. 2.4 show a different behavior of T^* depending on the considered fracture density and flow regime. When T^* increases from 0 to 1, the temperature

of the extracted fluid varies from the initial temperature in the system to the temperature of the injected fluid. This shows the progressive impact of the cooled injected fluid on the temperature of the extracted fluid due to the propagation of the cold front from the injection to the extraction wells. For *Fast Flows* (Fig. 2.4a), increasing the fracture density from $DFN1a$ to $DFN3a$ results in delaying the variations of T^* , showing that the cold front reaches the extraction well at longer times when considering larger fracture densities. In this case, the complexity and density of the fracture networks determine the propagation of the cold front across the domain and increasing the fracture network density implies an increase of the time required to propagate from the left to right sides of the domain. Conversely, for *Slow Flows* (Fig. 2.4b), the impact of the cold front on the production well is delayed when the fracture density decreases. In this case, the properties of the matrix blocks have a more important impact on the cold front propagation than the fracture network properties. For a small fracture densities ($DFN1a$), the cold front can propagate far away in the matrix without reaching a fracture, implying that this front reaches the extraction well at very large times. Increasing the fracture density ($DFN2a$ and $DFN3a$) implies that the cold front propagation inside the matrix is limited by the presence of fractures, which results in reaching the exploitation well at smaller times. These results show that the impact of the geological structures on the propagation of a cold front depends on the hydraulic regime, as these structures determine if heat transfer is controlled by the fracture network properties or the size of the matrix blocks.

Converting the previous results into PDFs enables us to study the anomalous behavior of heat transfer in our simulations. As demonstrated by the heavy tails observed in Fig. 2.5, this anomalous behavior occurs for both *Fast Flows* (Fig. 2.5a) and *Slow Flows* (Fig. 2.5b) configurations. This is mostly due to the contrast between the fracture and matrix properties, as these structures are responsible for fast and slow heat propagation across the domain, respectively. However, the results presented in Fig. 2.4 reveal that this anomalous behavior is also related to the heterogeneities of each structure (fracture networks and matrix blocks) whose importance

is determined by the hydraulic conditions. For *Fast Flows*, the fracture network complexity impacts the observed anomalous behavior. In this case, there is no impact of the matrix block heterogeneities as heat conduction inside these blocks is not limited by their size. Conversely, for *Slow Flows*, the matrix block size distribution impacts the observed anomalous behavior as heat conduction is limited by the size of these blocks.

2.5.2 Performance of geothermal systems

Figure 2.6 depicts the impact of both fracture density and fractal dimension on the performance of geothermal systems. The fracture networks with small fracture densities are not sensitive to the fractal dimension for both *Fast Flows* (Fig. 2.6a) and *Slow Flows* (Fig. 2.6b) conditions. This is due to the corresponding interconnected fracture networks which present small differences when changing the fractal dimension from 1 (Fig. 2.2a) to 1.1 (Fig. 2.2b) and no differences from 1.1 to 1.2 (Fig. 2.2c) and 1.3 (Fig. 2.2d). This shows the limitation of characterizing geothermal reservoirs only from core sampling as the related data do not give information on the connectivity of the domain. In terms of geothermal performance, this implies that reservoirs with different fracture network properties might have a nearly identical performance.

As the fracture density increases, from *DFN1* to *DFN3*, the impact of the fractal dimension D on the geothermal performance P_f depends on the hydraulic regime. For *Fast Flows* conditions (Fig. 2.6, left column), D does not have a significant impact on P_f , which is equal to 0 for times larger than 10^8 sec. For *Slow Flows* conditions (Fig. 2.6, right column), D has a significant impact for the largest fracture density considered in this study (*DFN3*, Fig. 2.6f): an increase in the fractal dimension, from *DFN3a* to *DFN3d*, decreases the reservoir's performance. For *Slow Flows*, $P_f = 0$ for times larger than 10^{12} , 10^{11} , and 10^{10} sec for the fracture networks *DFN1* (Fig. 2.6b), *DFN2* (Fig. 2.6d), and *DFN3* (Fig. 2.6f), respectively. This shows that increasing the fracture density causes the performance to decrease.

The different behavior of P_f for *Fast Flows* and *Slow Flows* conditions is related to the structural heterogeneities that control heat transfer in fractured domains. As demonstrated in Section 2.5.1, the fracture network and matrix block heterogeneities are determinant for *Fast Flows* and *Slow Flows* conditions, respectively, and, as demonstrated in Fig. 2.2, increasing the fracture density and fractal dimension results in more complex structures with more important heterogeneities. Therefore, broader distributions of the matrix block size are observed with the presence of small blocks that limit heat conduction in the matrix and reduce the performance of the systems.

2.6 Conclusion

Quantitative understanding of heat transfer in heterogeneous fractured media is necessary for economically feasible harvesting of geothermal energy. We used a mesh-free particle tracking method to model heat transfer in fractured geothermal reservoirs. This approach is capable of handling realistic discrete fracture networks and has computational efficiency that significantly exceeds that of standard (mesh-based) numerical methods. This enables us to conduct a series of two-dimensional heat transfer simulations for a large range of fracture network properties and experimental conditions and to interpret the corresponding results in terms of anomalous heat transfer and geothermal performance of reservoirs.

Our analysis leads to the following major conclusions.

1. Depending on hydraulic conditions, the propagation of a cold front across fractured domains is controlled by either the fracture network (*Fast Flows*) or matrix block (*Slow Flows*) properties.
2. The contrast of properties between fractures and matrix results in anomalous (non Fourier-like) behavior of heat transfer, which is enhanced by heterogeneity of the fracture networks (*Fast Flows*) and matrix blocks (*Slow Flows*).

3. For small fracture densities ($C = 2.5$), different values of the fractal dimension ($D = [1, 1.3]$) can lead to identical interconnected fracture networks with similar geothermal performance.
4. In fractured domains with large fracture density ($C = 6.5$) and fractal dimension ($D = 1.3$), a broad distribution of the matrix block size is obtained with the presence of small blocks that reduce the geothermal performances under *Slow Flows* conditions.
5. Over a wide range of fracture densities and fractal dimensions, the heat transfer significantly deviates from the Fourier law, giving rise to anomalous effective behavior characterized by long tails.

Although the low-computational cost of our method is attractive, some improvements could be introduced in future studies. These include incorporation of heterogeneity of matrix properties, implementation of two-dimensional convection by means of the analytical solutions developed by [Ruiz Martinez et al., 2014], and extensions to three-dimensional conditions.

In the latter case, the modeled fractures will be represented as two-dimensional elements and the impact of the domain and structure dimensionality could be studied by progressively improving our model. For example, representing the fractures as rectangles with a one-dimensional flow [Lee et al., 2001, e.g.,] will allow us to evaluate the impact of the fracture-network dimensionality. In comparison with two-dimensional simulations, the larger number of advective paths connecting the domain borders in three dimensions should lead to a larger distribution of the advection times spent in the fractures. These fractures could also be represented as ellipses [de Dreuzy et al., 2013, e.g.,] in which the heterogeneous flow velocity fields expand the distribution of advective times in comparison with the one-dimensional flow representation. As flow velocity in the fractures impacts heat propagation in both fractures and matrix, we also expect broader distributions of temperature of the extracted fluid with a significant anomalous behavior.

Finally, this study could be extended to more complex configurations where, for example, the impact of heterogeneous fracture apertures and randomly distributed fracture angles could be considered. In order to evaluate the interest of representing different levels of heterogeneity, our work is related to the uncertainty in site characterization [de Barros et al., 2012, Ezzedine, 2010] with Monte Carlo simulations.

ACKNOWLEDGEMENTS

The text of this chapter contains reprint of the material as it appears in the publication “Particle methods for heat transfer in fractured rocks” in the *Transport in Porous Media*, 115:311-326. 2016. Gisladdottir, V., Roubinet D., Tartakovsky D.. The dissertation author was the primary investigator and author of this article.

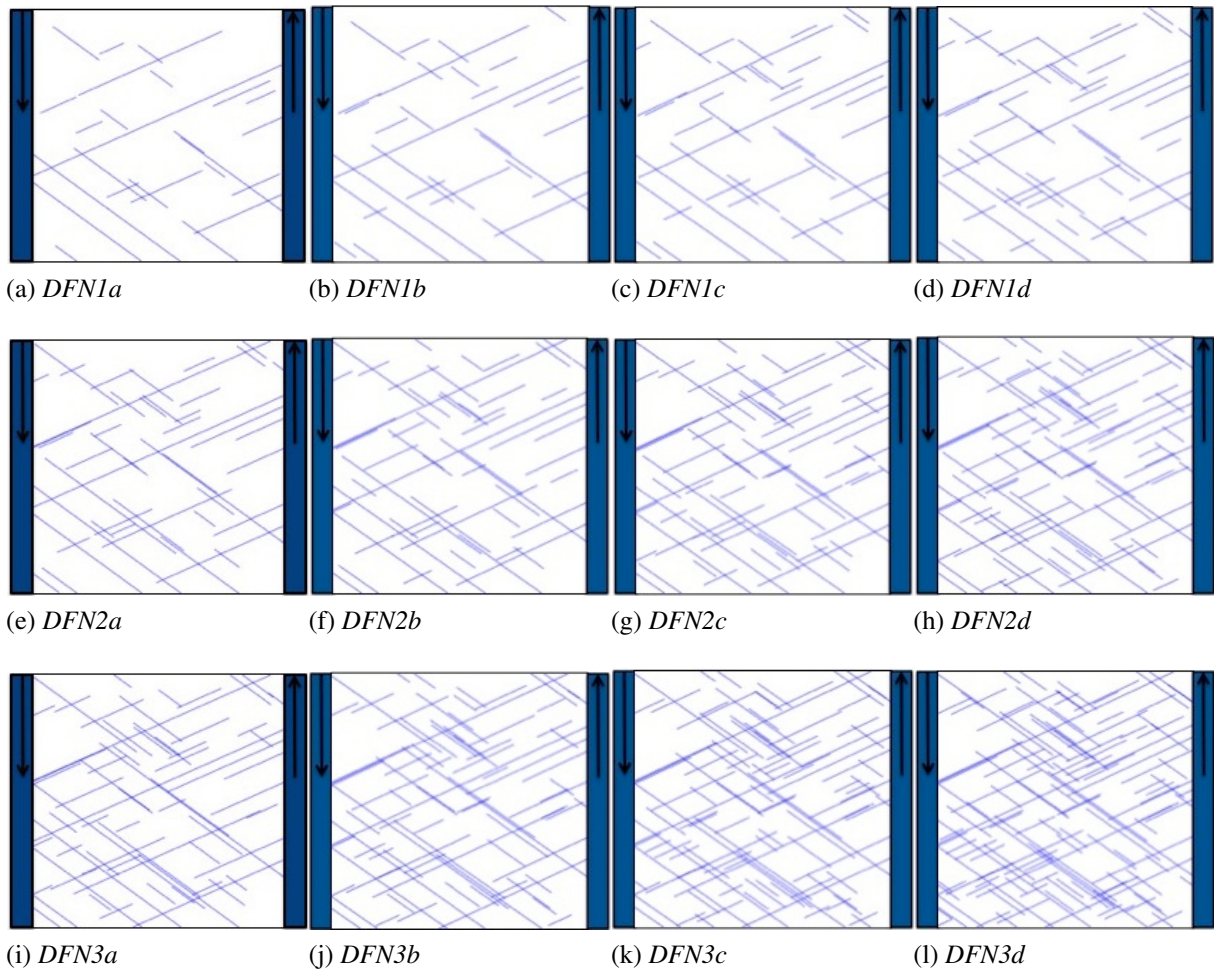


Figure 2.1: Fracture networks generated with the fracture network parameters presented in Table 2.1. The blue rectangles on the left and right sides of the domains represent the injection and extraction wells of the geothermal systems, respectively.

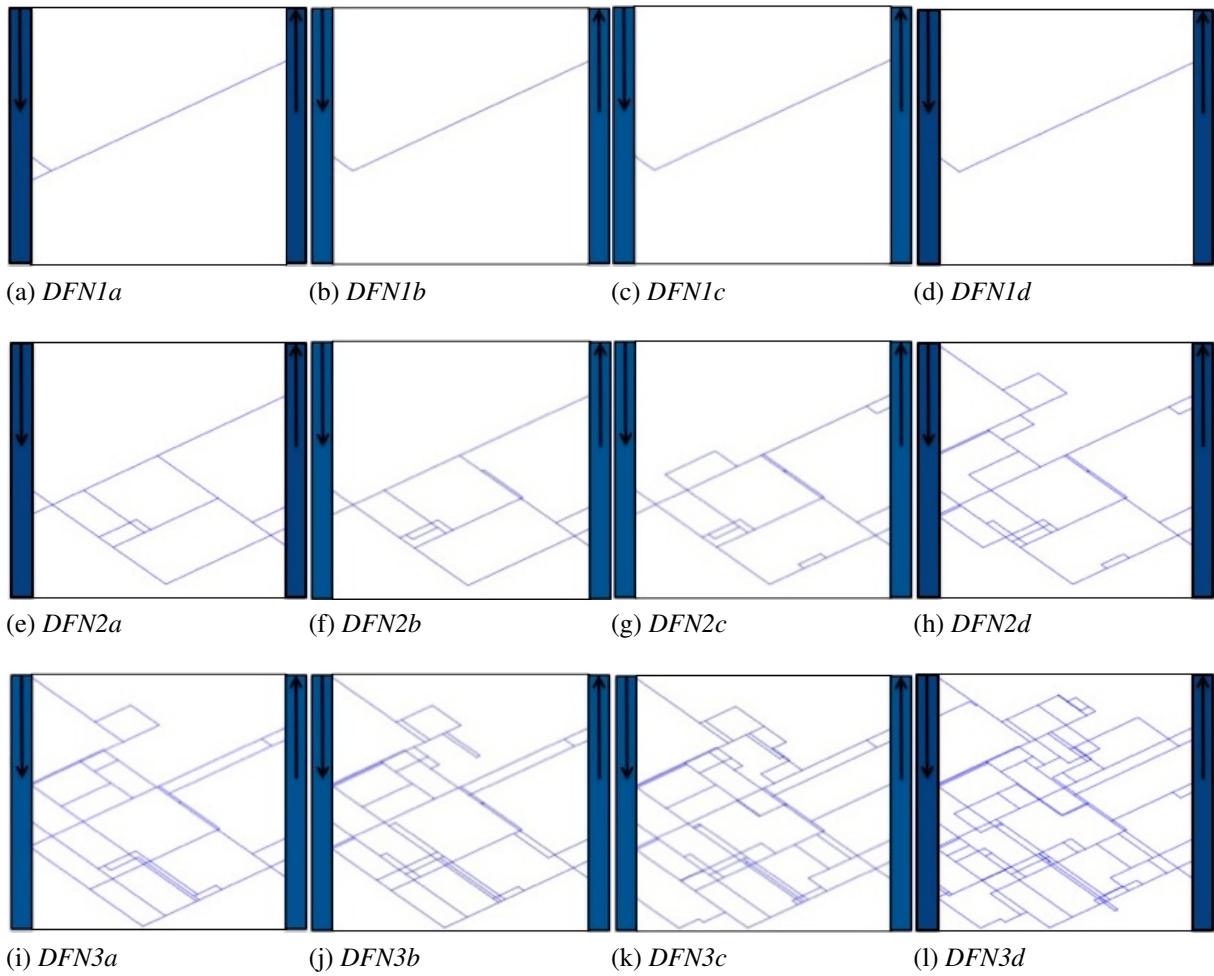
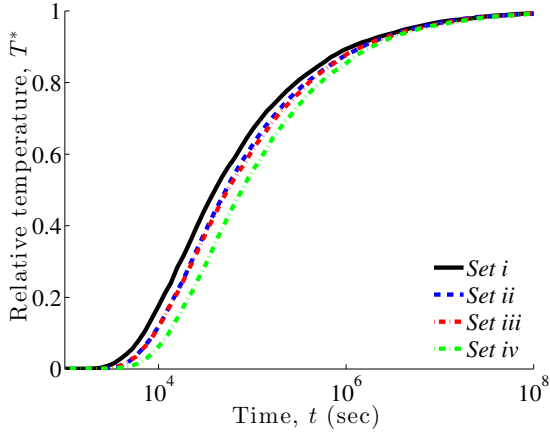
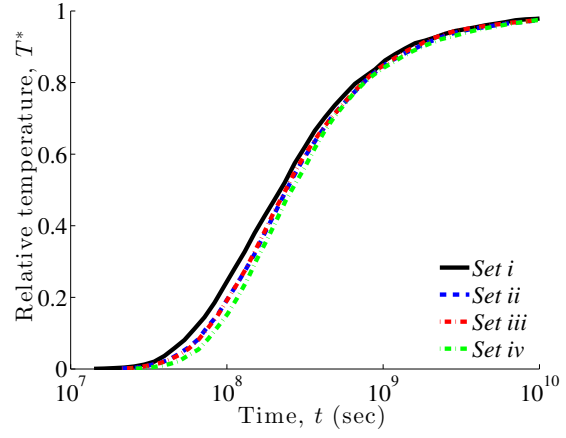


Figure 2.2: Interconnected fracture networks related to the fracture networks presented in Fig. 2.1 and connecting the injection and extraction wells.

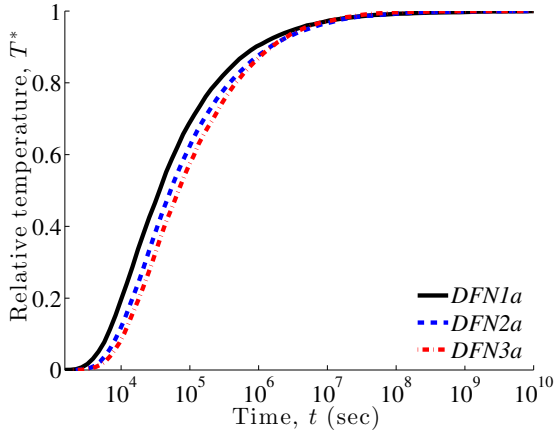


(a) Fast Flows

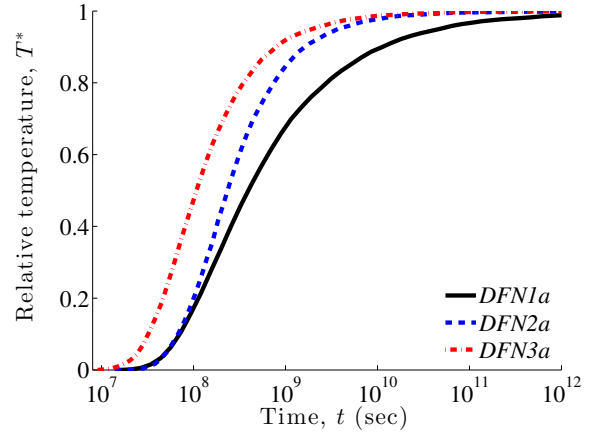


(b) Slow Flows

Figure 2.3: Temporal variability of the relative temperature T^* in fracture network $DFN2a$ with fractal dimension $D = 1$, for parameter sets (i)–(iv) in Table 2.2.

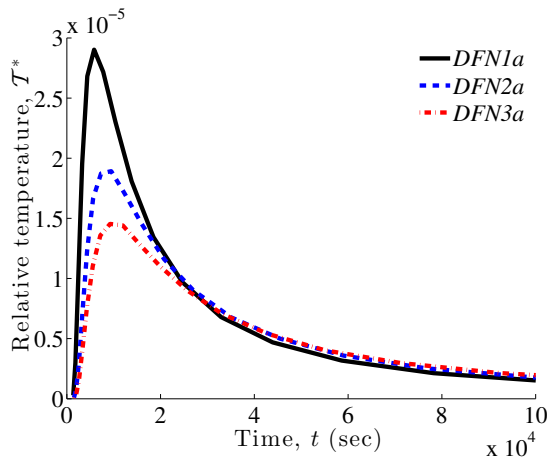


(a) *Fast Flows*

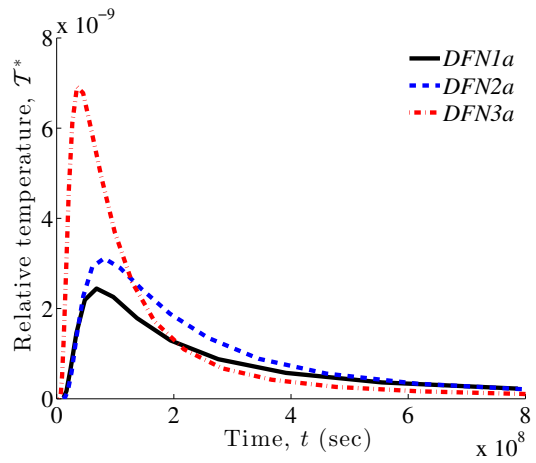


(b) *Slow Flows*

Figure 2.4: Temporal variability of the relative temperature T^* in fracture networks $DFN1a$, $DFN2a$, and $DFN3a$ (see Fig. 2.2), for the matrix properties from data set (ii) in Table 2.2 and (a) *Fast Flows* and (b) *Slow Flows* conditions.



(a) *Fast Flows*



(b) *Slow Flows*

Figure 2.5: Temporal variability of the relative temperature T^* in fracture networks $DFN1a$, $DFN2a$, and $DFN3a$ (see Fig. 2.2), for the matrix properties from data set (ii) in Table 2.2 and (a) *Fast Flows* and (b) *Slow Flows* conditions.

Table 2.1: Parameters used to generate alternative fracture networks.

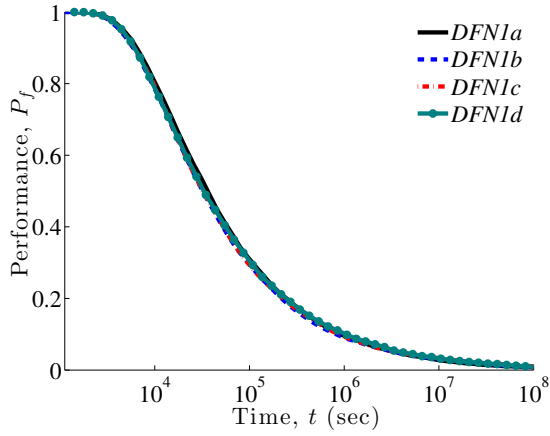
| | C [-] | D [-] | θ_1 [°] | θ_2 [°] | r_0 [m] | b [m] |
|--------------|---------|---------|----------------|----------------|-----------|--------------------|
| <i>DFN1a</i> | 2.5 | 1 | 25 | 145 | 10^{-1} | 5×10^{-4} |
| <i>DFN1b</i> | 2.5 | 1.1 | 25 | 145 | 10^{-1} | 5×10^{-4} |
| <i>DFN1c</i> | 2.5 | 1.2 | 25 | 145 | 10^{-1} | 5×10^{-4} |
| <i>DFN1d</i> | 2.5 | 1.3 | 25 | 145 | 10^{-1} | 5×10^{-4} |
| <i>DFN2a</i> | 4.5 | 1 | 25 | 145 | 10^{-1} | 5×10^{-4} |
| <i>DFN2b</i> | 4.5 | 1.1 | 25 | 145 | 10^{-1} | 5×10^{-4} |
| <i>DFN2c</i> | 4.5 | 1.2 | 25 | 145 | 10^{-1} | 5×10^{-4} |
| <i>DFN2d</i> | 4.5 | 1.3 | 25 | 145 | 10^{-1} | 5×10^{-4} |
| <i>DFN3a</i> | 6.5 | 1 | 25 | 145 | 10^{-1} | 5×10^{-4} |
| <i>DFN3b</i> | 6.5 | 1.1 | 25 | 145 | 10^{-1} | 5×10^{-4} |
| <i>DFN3c</i> | 6.5 | 1.2 | 25 | 145 | 10^{-1} | 5×10^{-4} |
| <i>DFN3d</i> | 6.5 | 1.3 | 25 | 145 | 10^{-1} | 5×10^{-4} |

Table 2.2: Physical properties of fractured rocks used to simulate heat transfer.

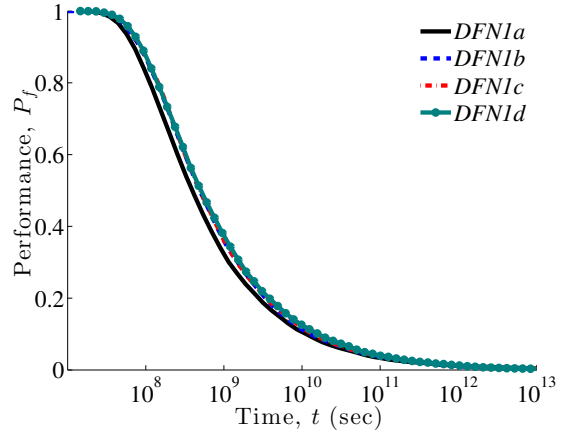
| Parameter set (i) | Values |
|-----------------------------------|---------------|
| Thermal conductivity [W/(m·°C)] | 1.5 |
| Rock density [kg/m ³] | 2700 |
| Rock heat capacity [J/(kg·°C)] | 920 |
| Parameter set (ii) | Values |
| Thermal conductivity [W/(m·°C)] | 2.1 |
| Rock density [kg/m ³] | 2650 |
| Rock heat capacity [J/(kg·°C)] | 1000 |
| Parameter set (iii) | Values |
| Thermal conductivity [W/(m·°C)] | 2 |
| Rock density [kg/m ³] | 2500 |
| Rock heat capacity [J/(kg·°C)] | 1000 |
| Parameter set (iv) | Values |
| Thermal conductivity [W/(m·°C)] | 2.5 |
| Rock density [kg/m ³] | 2500 |
| Rock heat capacity [J/(kg·°C)] | 880 |

Table 2.3: The Kolmogorov-Smirnov statistic \mathcal{S}_{KS} for fracture networks characterized by their fractal dimension D and fracture density C .

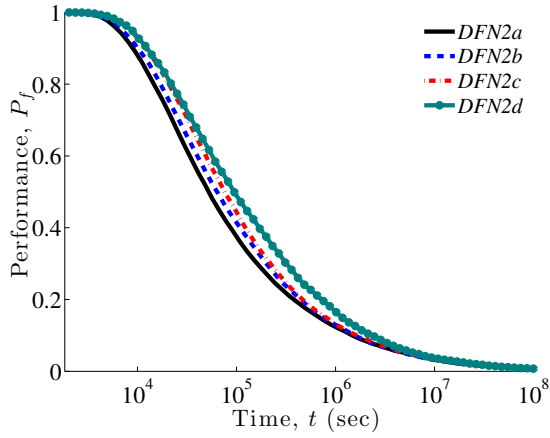
| Fractal dimension, D | Fracture density, C | Kolmogorov-Smirnov statistic, \mathcal{S}_{KS} |
|------------------------|-----------------------|--|
| 1.0 | 2.5 | 0.472 |
| 1.0 | 3.5 | 0.470 |
| 1.0 | 4.5 | 0.456 |
| 1.0 | 5.5 | 0.451 |
| 1.0 | 6.5 | 0.447 |
| 1.3 | 2.5 | 0.466 |
| 1.3 | 3.5 | 0.470 |
| 1.3 | 4.5 | 0.473 |
| 1.3 | 5.5 | 0.448 |
| 1.3 | 6.5 | 0.403 |



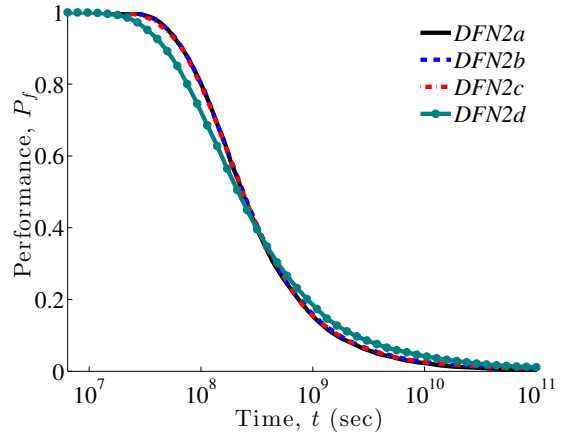
(a) Fast Flows, DFN1



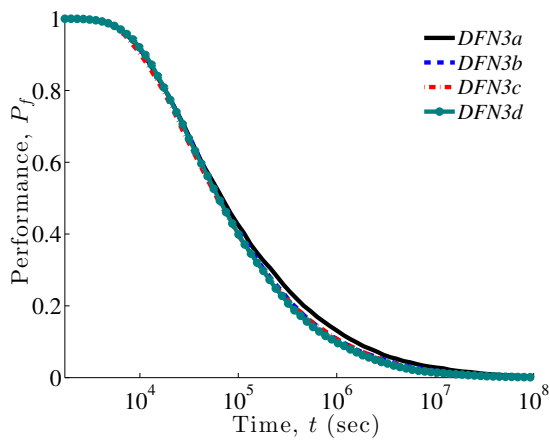
(b) Slow Flows, DFN1



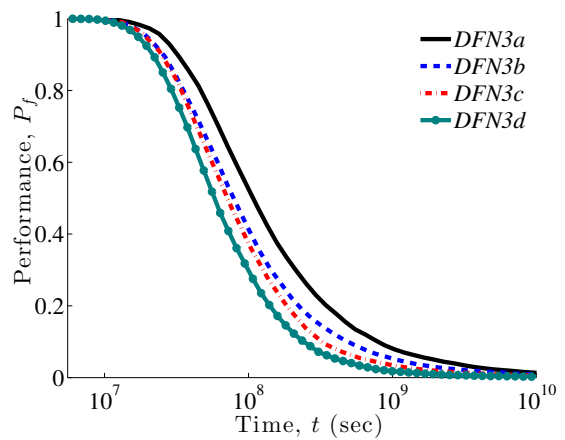
(c) Fast Flows, DFN2



(d) Slow Flows, DFN2



(e) Fast Flows, DFN3



(f) Slow Flows, DFN3

Figure 2.6: Temporal variability of the geothermal performance P_f of the fracture networks presented in Fig. 2.2 with the matrix properties from data set (i) in Table 2.2, for the *Fast Flows* (left column) and *Slow Flows* (right column) conditions.

Chapter 3

Efficient simulations of heat transfer in fractured rocks

3.1 Introduction

Models of heat transfer in fractured media require information about hydraulic and thermal properties of both a fluid-filled fracture network and the ambient rock matrix. Features germane to geothermal reservoirs include (i) a strong contrast between the fracture and matrix properties resulting in advective and conductive mechanisms in the fractures and matrix, respectively; (ii) topological properties of a fracture network that determine the spatial extent of a heat extraction area; and (iii) fracture-matrix heat flux exchanges that control the geothermal performances.

Fracture networks often have a hierarchical or fractal structure [Sahimi, 1993]. There are many different ways to generate such networks for reservoir modeling. One example of a fractal network, commonly used to simulate solute transport in hierarchically fractured rocks, are Sierpinski lattices [Doughty and Karasaki, 2002], [Roubinet et al., 2013a]. Another example is a Watanabe-Takahashi network [Watanabe and Takahashi, 1995], which often captures key

attributes of geothermal reservoirs. Both have been successfully employed in reservoir models, where coupled fluid flow and solute/heat transport are induced by either ambient or forced hydraulic conditions. However, fractal networks with same geometrical parameters (e.g., fractal dimension) and similar physical and/or hydraulic properties can look very different from each other [Roy et al., 2007]. This complicates both in-situ characterization of geothermal systems and identification of their "realistic" conceptual representations.

The presence of fractures on a large range of spatial scales and the strong contrast in properties between fractures and matrix imply that fractured reservoirs exhibit multi-scale heterogeneity. They also suggest that standard numerical models of coupled fluid flow and heat transport processes in these domains have (prohibitively) large computational cost. To tackle this challenge, we have introduced a mesh-free particle method, which was used to demonstrate the anomalous (non-Fourierian) behavior of heat transfer in fractured rocks [Gisladdottir et al., 2016]. Here, we use this method to simulate heat extraction in various hierarchical fracture networks at a small computational cost. Our main objectives are to compare the geothermal performances for different types of fractal networks and to analyze the impact of network properties on the computation efficiency of our method. For this purpose, we consider Sierpinski lattices and Watanabe-Takahashi networks with identical fracture density and smallest fracture length. Our analysis of the Sierpinski and Watanabe networks reveals that (i) for hydraulic regimes characterized by slow flow velocities (i.e., ambient hydraulic conditions), the geothermal performances of the two network classes differ by close to an order of magnitude, and (ii) for hydraulic regimes characterized by fast flow velocities, the differences are much smaller and the geothermal performances are of the same order of magnitude. These different behaviors are mostly due to the differences in topological properties of the Sierpinski or Watanabe networks. Additionally, the CPU efficiency is not greatly affected by the topological properties (i.e. Sierpinski vs. Watanabe), however depending on the hydraulic regime fracture density may or may not increase the computational cost. For an example of hydraulic parameters used in geothermal

studies the fracture density increase did not increase computational cost.

3.2 Problem formulation

3.2.1 Fracture networks

Since the introduction of the notion of fractal geometry to geological structures [Mandelbrot, 1982] and [Turcotte, 1997], the idea has gained support that fracture networks often have a hierarchical or fractal structure [Sahimi, 1993]. Multiple fracture networks have been used for transport modeling. Sierpinski lattices are an example of synthetic fractal fracture. They have been used to simulate dynamic processes in hierarchically fractured rocks [Doughty and Karasaki, 2002], [Roubinet et al., 2013a]. Watanabe and Takahashi (1995) have introduced an alternative fractal network, which captures geothermal reservoir characteristics observed in the field, using only a few parameters that can be obtained from borehole data. In Sierpinski networks, a flow domain is subdivided into nine equal squares by two orthogonal sets of fractures. For a domain of size of L , each fracture spacing, both between the fractures and the distance from the domain border, is $L/3$. This is referred to as the template. Then N_{sq} squares are filled with the template. When the length of the template's set of orthogonal fractures is $L/3$ (and the fracture spacing is $L/3^2$), this is known as level 2. The process is then repeated until a desired level is reached. An example of a level-3 Sierpinski lattice with $N_{sq} = 3$ and orthogonal fracture set with smallest fracture length equal to $L/3^3$ is shown in Figure 3.1. In Watanabe-Takahashi networks, the number of fractures, N_f , and the normalized length, r_i , of the i th fracture ($i = 1 \dots N_f$) are related by

$$N_f = \text{int}(C/r_0^D), \quad r_i = C/i^{1/D} \quad (3.1)$$

where D is the fractal dimension, and the function $int(x)$ rounds x up to the next integer. The fracture density C and the smallest fracture length r_0 can be estimated from a core sample. The fracture aperture b is constant and the same for all fractures. A fracture network is generated by assigning each midpoint of a fracture pair a random variable. There is an equal probability that the angle between the pair of fractures takes on two prescribed values, θ_1 or θ_2 . To facilitate comparison of the Sierpinski and Watanabe networks, both are assigned the same fracture density and smallest fracture length. The former is defined as the cumulative length of fractures per area of the domain [Singhal and Gupta, 2010],

$$\rho = \sum_i r_i / L^2 \quad (3.2)$$

For the Sierpinski lattices the length of the smallest fracture element is used, while for the Watanabe network the smallest fracture length is r_0/L .

3.2.2 Fluid flow and governing equations

We consider steady-state laminar flow of an incompressible fluid in fractures embedded into impervious surrounding rock matrix. Each fracture is formed by two parallel smooth plates, resulting in the parabolic (Poiseuille) velocity profile and the average flow velocity u given by

$$u = -\left(\frac{\rho_l g b^2}{12\mu} J\right) \quad (3.3)$$

where ρ_l and μ are, respectively, density and dynamic viscosity of the fluid; J is the hydraulic head gradient along the fracture; and g is the gravitational acceleration constant. By applying equation 3.3 to each fracture segment and enforcing mass conservation at the fracture junctions, a linear system $\mathbf{A}=\mathbf{h}\mathbf{b}$ is formed where \mathbf{h} is the vector of the (unknown) hydraulic heads at fracture junctions [Long et al., 1982, De Dreuzy et al., 2001]. With a known global pressure

gradient imposed on the boundaries of the domains, the linear system is solved providing the hydraulic heads necessary to compute the average flow velocity in each fracture of the network. The particle-based method described in Section 3.2.3, and presented in Gisladdottir et al. (2016), models heat transfer in fractured media by using a solution for a single fracture embedded in an infinite matrix as a base for a probabilistic model. Heat transfer in a single fracture of aperture, b , and semi-infinite length is described by coupled boundary-value problems. One, consisting of an advection-dispersion-equation (ADE), governs temperature in the fracture, $T^f(x, x, t)$. The other, involving a diffusion equation (DE), represents temperature in the matrix, $T^m(x, z, t)$. The continuity of temperature and heat flux is enforced at the fracture-matrix interfaces, coupling these two boundary-value problems. Initially the temperature throughout the domain, both in the fracture and the matrix, is equal to T_0 . The same temperature is prescribed along all external boundaries. The temperature of the injected fluid is equal to T_{inj} .

3.2.3 A particle-based algorithm for heat transfer

To ascertain the impact of network model selection (e.g., Sierpinski vs. Watanabe networks) and to evaluate the impact of global network properties on heat transfer, we use the mesh-free particle method presented by Gisladdottir et al. [2016]. For the sake of completeness, we reproduce it here. The method spans three scales: i) the fracture-matrix scale where heat transfers by advection in the fractures and conduction in the infinite matrix, ii) the matrix-block scale where heat conduction is limited by neighboring fracture, and iii) the fracture-network scale where heat flux conservation is enforced at each fracture intersection and depends on the corresponding flow rate distribution. At the fracture-matrix scale, an approximate analytical solution of the boundary-value-problems formulated in Section 3.2.2 takes the form (Tang et al., 1981)

$$T^f(x, t) = T_{inj} \operatorname{erfc} \left(\frac{\phi_m \sqrt{D_T^m x}}{2ub \sqrt{t - x/u}} \right) \quad (3.4)$$

It relies on the following simplifications: (i) longitudinal dispersion in the fracture is assumed to be negligible in comparison with convection, (ii) the ADE equation is averaged over the fracture aperture, and (iii) heat transfer in the matrix is assumed to be one-dimensional, perpendicular to the fracture. This analytical solution is inverted in order to evaluate the time t_{diff} spent by a "particle" in the matrix for a given displacement in the fracture. To do so, Equation 3.4 is used as a probabilistic model, which replaces T^f with a uniform random generator R defined on the interval $[0,1]$, and the result is inverted to compute corresponding random realization of t_{diff} . At the matrix-block scale, the effects of potential neighboring fractures are taken into account by considering the case of a fracture f_i with one fracture on each side f_1 and f_2 at distance l_1 and l_2 , respectively. For a particle leaving fracture f_i and diffusing into the matrix, we define P_t^1 , the probability of reaching fracture f_1 without crossing fracture f_2 and P_t^2 , the probability of reaching fracture f_2 without crossing fracture f_1 . These first-passage-time probabilities are given analytically in the Laplace space [Feller, 1954], and back-transformed into the time domain using numerical inversion with, e.g., the Stehfest [1970] algorithm. Next, we generate P_{transfer} , the probability for a particle to transfer to one of the neighboring fractures with an associated transfer time t_{transfer} smaller than the maximum diffusion time t_{diff} , as

$$P_{\text{transfer}} = P_{\text{transfer}}^1(t_{\text{transfer}} \leq t_{\text{diff}}) + P_{\text{transfer}}^2(t_{\text{transfer}} \leq t_{\text{diff}}) \quad (3.5)$$

Once the value of P_{transfer} is evaluated, we pick a random number U from a uniform distribution on the interval $[0,1]$. If U is larger than P_{transfer} , the particle does not transfer to the neighboring fractures, otherwise it does and the transfer time t_{transfer} is found by solving $P_{\text{transfer}} = U$. The particle transfers to f_1 if the condition $U/U_{\text{max}} > l_1/(l_1+l_2)$ holds with $U_{\text{max}} = P_{\text{transfer}}$, otherwise it transfers to f_2 . At the fracture-network scale, if a particle reaches a fork intersection at the end of the fracture, the fracture to which it transfers is determined from heat flux conservation. The latter accounts for the intersection configuration and flow rate distribution as follows. The

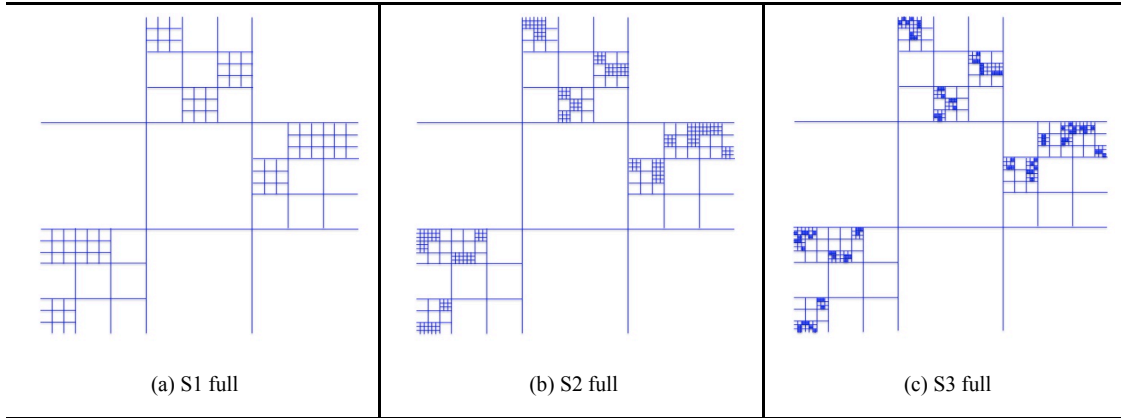


Figure 3.1: Sierpinski networks with levels $M = 3$ (S1, left), $= 4$ (S2, center), and $= 5$ (S3, right).

particles enter fractures with positive flow taking into account full mixing and streamline routing rules (Hull, 1986 and Berkowitz, 1994). Assuming that complete mixing takes place, the probability of a particle to enter into a fracture is the ratio of flow rate in the considered fracture to the sum of the flow rates leaving the considered intersection. If a particle can enter two fractures, the particle enters the fracture with dominant flow [Le Goc, 2009b].

3.3 Simulation set up

In order to investigate the importance of network model selection, we consider the Sierpinski and Watanabe fracture networks embedded into a square matrix domain with side lengths of 100 m. Figure 3.1 shows Sierpinski lattice networks S1, S2, and S3 with $N_{sq}=3$ and level $M=3, 4,$ and $5,$ respectively. The fracture densities and smallest length elements of these networks are collated in Table 3.2.

For each of the Sierpinski networks S1, S2, and S3, there exists a Watanabe network with a similar fracture density (within 2% difference) and the same smallest fracture length (Table 3.2). Those networks are labeled Watanabe network W1, W2, and W3, respectively. They are shown in Figure 3.2 with the fractures generated by Equation 3.1 (top row) and the backbone

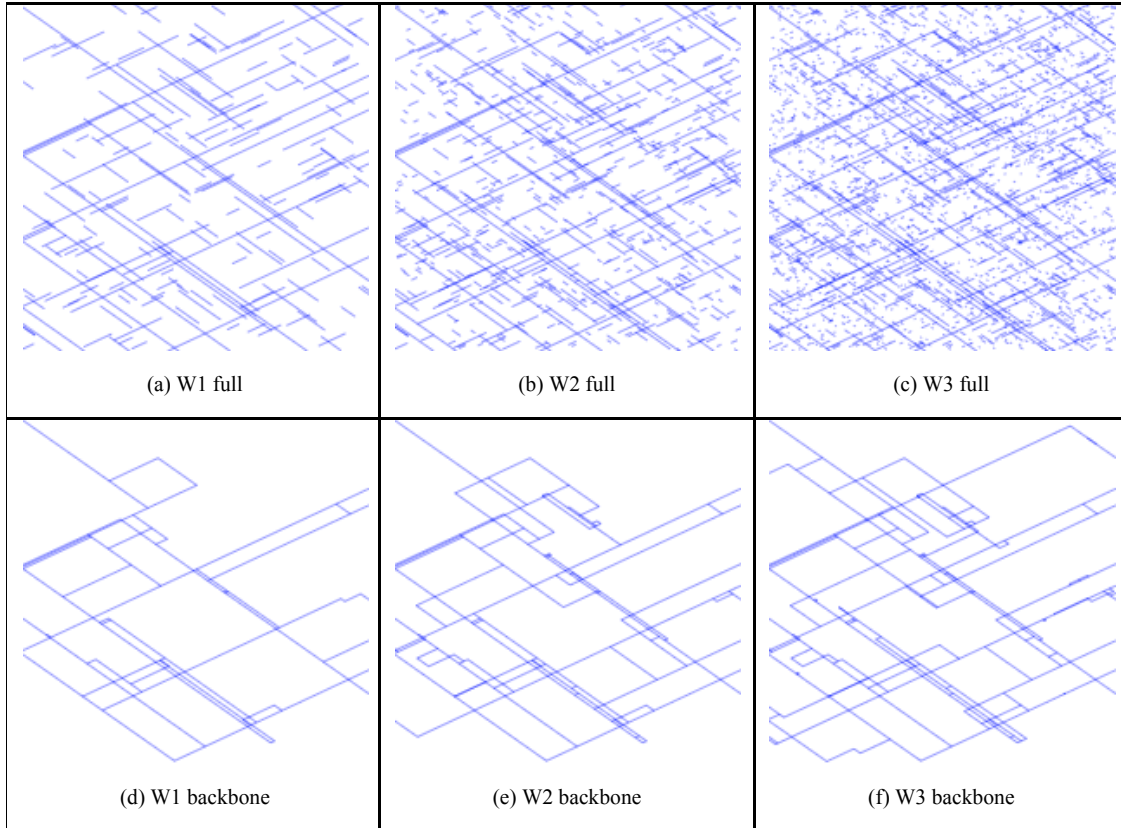


Figure 3.2: Top row: three Watanabe networks generated by equation (1) for the parameters in Table 3.2. Bottom row: backbones of these networks.

of those fracture networks (bottom row). The Watanabe networks have the fractal dimension D whose values are found in the natural environment [Main et al., 1990], [Scholz et al., 1993] and is employed for geothermal characteristic networks [Watanabe and Takahashi, 1995]. For both networks only the fractures belonging to their respective backbones are identified based on the velocity field.

An injection well spans the left side of the computational domain, and the extraction well represents its right side. Fluid flow takes place from left to right through the interconnected network. To show the robustness of the prediction we look at two different hydraulic regimes between two boreholes set up for the geothermal exploitation. The first regime, called Fast flow, is defined with a head gradient of 1.25 MPa and is employed in existing studies on geothermal systems [Suzuki et al., 2015]. The second regime, called Slow flow, is defined with a head

gradient set to 10^{-2} MPa and is used for comparison. Bottom and top borders of the domain are considered to have no-flow boundaries. The flow velocity fields are generated as described in Section 3.2.2 with fluid density and dynamic viscosity, $\rho_v = 10^3$ kg and $\mu = 10^{-3}$ kg/(m s), respectively. The physical properties are thermal conductivity, $k = 2.1$ W/(m·°C); rock density, $\rho_f = 2650$ kg/m³; and rock heat capacity, $c_p = 1000$ J/(kg·°C). The Peclet number is defined as $Pe = (L \cdot u_{ave})/\alpha$ where $L=100$ m is the length of the domain; u_{ave} is the average flow velocity in the network (Table 3.1); and α is the thermal diffusivity $\alpha = k/(\rho_f c_p)$.

Table 3.1: Global parameters for Sierpinski and Watanabe networks generation.

| | Fracture Density [-] | Level M [-] | Frac. Density parameter, C [-] | Smallest fracture length [m] |
|-----------|-------------------------|------------------|-------------------------------------|---------------------------------|
| <i>S1</i> | 0.109 | 3 | | 3.7 |
| <i>S2</i> | 0.147 | 4 | | 1.23 |
| <i>S3</i> | 0.185 | 5 | | 0.41 |
| <i>W1</i> | 0.109 | | 45 | 3.7 |
| <i>W2</i> | 0.149 | | 22.3 | 1.23 |
| <i>W3</i> | 0.184 | | 13.87 | 0.41 |

Reporting on geothermal reservoirs is often done in the form of $P_f = 1 - T$ where the minimum efficiency of the system is represented as $P_f = 0$ because the temperature of the extracted fluid is equal to the temperature of the (here cooler) injected fluid. Therefore the maximum efficiency of the system is represented as $P_f = 1$ corresponding to cases where the temperature of the extracted fluid is equal to the (here warmer) initial temperature of the system. Figure 3.3 shows the temporal profiles $P_f(t)$ for all six networks for both hydraulic regimes Fast flow and Slow flow. These simulations were done using $5 \cdot 10^3$ particles and they are similar to simulations performed with 10^4 .

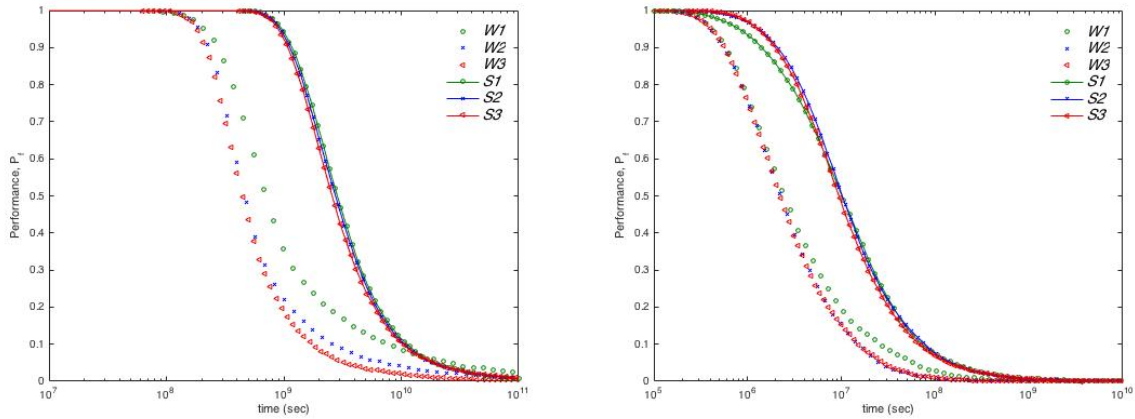


Figure 3.3: The Performance of the system as a function of time for heat transport between two boreholes 100 m apart across fracture networks: S1, S2, and S3 (Figure 1) as well as W1, W2, and W3 (Figure 2) for Slow flow (left) and Fast flow (right)

3.4 Results and discussion

In Figure 3.3 we look at the performance of the system over time at the extraction borehole on the right-hand side of the domain for all six interconnected networks S1, S2, S3, W1, W2, and W3 presented in Figure 3.1 and Figure 3.2. For Slow flow (left), the Watanabe networks have significantly faster drop in the performance, almost an order of magnitude, than the Sierpinski networks in which the particles appear to spend more time in the matrix. This is due to the fact that there are far more preferential pathways, fractures that span the entire domain left to right, in the Watanabe networks. When performing a simulation with the same hydraulic head on those two networks, such as here, it results in higher average velocity in the Watanabe networks (due to higher number of preferential pathways) than the Sierpinski networks as is shown in Table 3.1. The increased velocity causes lower probability for the particles to enter the matrix. For both the Watanabe network and the Sierpinski network as the fracture density increases the arrival times decrease due to the limitations of the matrix block. Although there is eventually a difference between W1 and W2, the performance is quite similar past the 50% drop

in the performance.

Table 3.2: Network flow velocity values for Sierpinski and Watanabe networks for Slow and Fast flow.

| Velocity m/s | Slow flow Ave | Slow flow Min | Slow flow Max | Fast flow Ave | Fast flow Min | Fast flow Max |
|-----------------|----------------------|-----------------------|----------------------|----------------------|----------------------|----------------------|
| <i>S1</i> | $6.37 \cdot 10^{-5}$ | $9.57 \cdot 10^{-7}$ | $3.05 \cdot 10^{-3}$ | $7.96 \cdot 10^{-2}$ | $1.20 \cdot 10^{-4}$ | $3.81 \cdot 10^{-1}$ |
| <i>S2</i> | $3.95 \cdot 10^{-4}$ | $4.11 \cdot 10^{-8}$ | $3.12 \cdot 10^{-3}$ | $4.94 \cdot 10^{-2}$ | $5.14 \cdot 10^{-6}$ | $3.90 \cdot 10^{-1}$ |
| <i>S3</i> | $2.31 \cdot 10^{-4}$ | $6.25 \cdot 10^{-10}$ | $3.15 \cdot 10^{-3}$ | $2.89 \cdot 10^{-2}$ | $7.82 \cdot 10^{-8}$ | $3.94 \cdot 10^{-1}$ |
| <i>W1</i> | $1.18 \cdot 10^{-3}$ | $2.96 \cdot 10^{-5}$ | $3.86 \cdot 10^{-3}$ | $1.47 \cdot 10^{-1}$ | $3.70 \cdot 10^{-3}$ | $4.82 \cdot 10^{-1}$ |
| <i>W2</i> | $1.16 \cdot 10^{-3}$ | $9.46 \cdot 10^{-6}$ | $3.35 \cdot 10^{-3}$ | $1.14 \cdot 10^{-1}$ | $1.18 \cdot 10^{-3}$ | $4.19 \cdot 10^{-1}$ |
| <i>W3</i> | $1.17 \cdot 10^{-3}$ | $6.00 \cdot 10^{-8}$ | $3.47 \cdot 10^{-3}$ | $1.47 \cdot 10^{-1}$ | $7.49 \cdot 10^{-6}$ | $4.34 \cdot 10^{-1}$ |

For the Fast flow (right) the velocity variation (Table 3.1) between the networks is not as high and hence the variance of the performance between Sierpinski and Watanabe networks is not as stark for the Fast flow regime. Yet again the Watanabe networks have faster drop in the performance than the Sierpinski networks, although the difference is not as dramatic. For the Watanabe networks, initially there is not a large difference between the performances for the different fracture density networks, although the lowest fracture density network W1's performance drops slightly faster to begin with. Eventually about approximately at the mean this trend reverses and the performance of W1 drops slower than for W2 and W3 where the highest fracture density network W3 has a faster drop in the performances. For Sierpinski lattices the low fracture density network S1 starts off with faster drop in performance but also reverses roles with the high-density fracture network S3 as time passes this happens slightly before reaching the mean. Over all the main features of the fracture network is of importance in the Fast flow and the matrix block only play a minor role and mostly somewhere after the mean of the performance drop. The Peclet numbers for networks S1-S3 and W1-W3 generated based on the average velocity presented in Table 3.1 and defined in Section 4.4 are on the $[6.95 \cdot 10^3 \ 1.88 \cdot 10^5]$ range for Slow flow regime and the $[3.15 \cdot 10^6 \ 2.35 \cdot 10^7]$ range for Fast flow regime both of which are advection dominant. To begin with the all three Watanabe networks have a similar performance

eventually past the 50% level of drop the W1 performance drops slower than the other two Watanabe networks. For the Sierpinski networks initially S1 performance drops faster than S2 and S3, who have similar drop, but once past the 50% performance drop this reverses. Although the difference is not as much S1's performance drops slower than the other two.

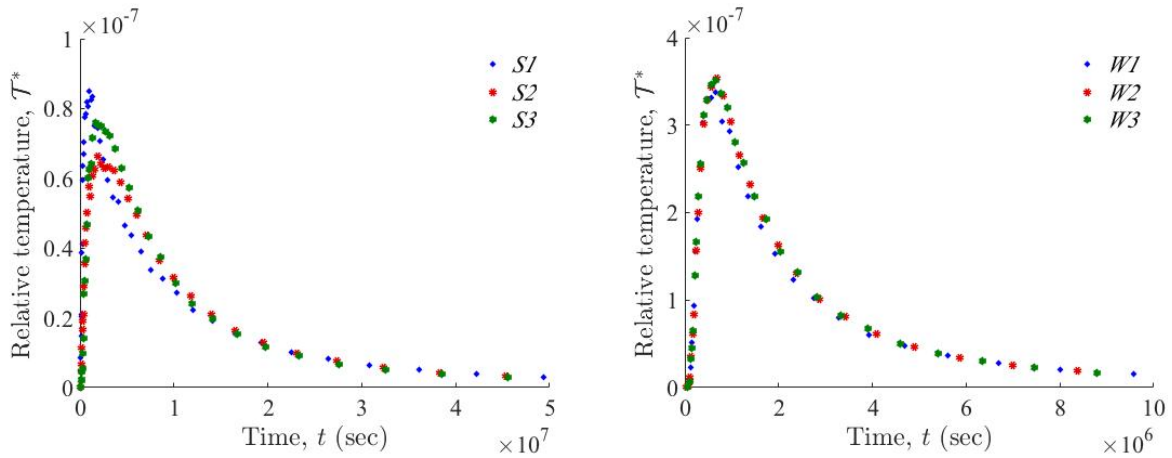


Figure 3.4: Temporal variability of the relative temperature of fracture networks (left) S1, S2, S3, (see Figure 1) and (right) W1, W2, and W3 (see Figure 2) for Fast flow hydraulic regime.

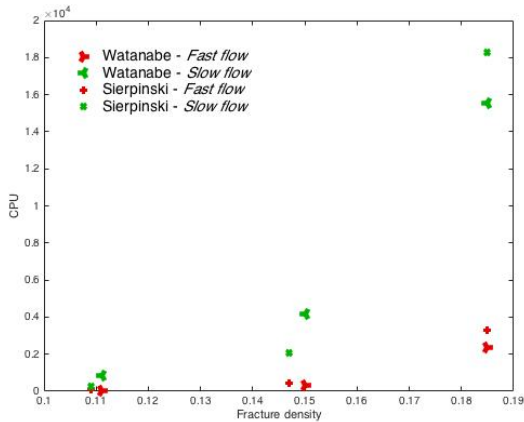


Figure 3.5: The CPU for the varying fracture density for the Watanabe and Sierpinski Networks for Fast flow and Slow flow.

To elucidate the anomalous (non Fourier like) nature of heat transfer in fracture rocks we define a relative temperature as the instantaneous temperature change of the injected fluid.

In Figure 4 we see the temperature distribution for the S1, S2, S3, W1, W2, and W3 for Fast flow and Slow flow regimes. These results are obtained by taking a PDF of the original CDF distribution of the arrival times. The heavy tail found in Figure 3.4 demonstrates that this anomalous behavior is found in for all of the Sierpinski and Watanabe networks in the Fast flow regime. Its presence is due to fracture properties as they influence fast heat propagation across the domain.

In Figure 3.5 we look at the computational cost of running the simulations of heat transport across our 100 m domain for the six networks S1, S2, S3, W1, W2, and W3 producing the results presented in Figure 3.5 as a function of their fracture density which is found in Table 3.2. For both the Sierpinski and the Watanabe networks there is significant higher CPU usage for Slow flow hydraulic regime for high fracture density networks. However in both case the increase is not significant for low fracture density networks. Interestingly enough for the hydraulic regime representative of those used in geothermal field studies Fast flow (Suzuki et al. 2015) increasing the fracture density does not increase computational cost, this applies to both Sierpinski and Watanabe networks.

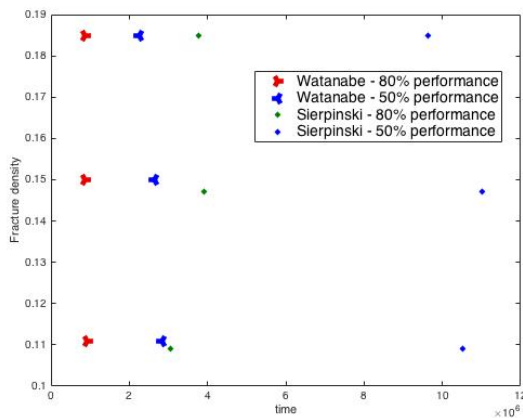


Figure 3.6: The temporal variation of the performance drop of the system over 100 m to levels of 80% and 50% for varying degrees of fracture density for Fast flow hydraulic regime.

From Figure 3.6 we conjure that the time it takes the performance drop of the system to level of 80% and 50% performance has more dependence on the type of fracture network than

the density of the network itself. There is more significant difference on the 50% performance drop between Watanabe and Sierpinski network then for the networks for 80% drop.

3.5 Conclusion

We use a computationally light mesh-free particle method to perform numerical simulations on discrete fracture networks representative of a fractured porous medium. The particle method is applied to two different networks, Sierpinski and Watanabe networks, with three sets of parameters for fracture density and smallest fracture length. For all six simulations, we have reported on performance of the system, in particular: pulse injection anomalous behavior; CPU expenditure; and levels at which we project 20% and 50% performance drops.

The results show that depending on hydraulic conditions, the propagation of a cold front across fractured domains is controlled by either the fracture network (Fast Flows) or matrix block (Slow Flows) properties. For fast flow both Sierpinski (S2 and S3) and Watanabe (W2 and W3) demon straight similar behaviors within in the network type although the density increases. However both of their lower density networks S1 and W1 very from their network type past the 50% performance drop, although S1 additionally varies from S2 and S3 to begin with. There is a stark contrast between the performance drop of all three Sierpinski and all three Watanabe networks. This in turn means that the performance drop of the system to levels of 80% and 50% are far more dependent on the type of network rather than fracture density for Fast flow hydraulic regime. The heat transfer significantly deviates from the Fourier law, over a wide range of fracture densities, giving rise to anomalous effective behavior characterized by long tails. Additionally the hydraulic regime has far more impact then the topological properties as for an example of a hydraulic regime used in geothermal field studies Fast flow the computational cost did not significantly increase with increased fracture density.

Our results demonstrate that our algorithm takes a fraction of the time that it would take

a mesh based numerical solutions of heat transfer equations. To further quantify the relative improvement we are engaged in further quantitative comparison of the particle method against a mesh method for a particular physical fracture example. Additionally, extending the studies to incorporate heterogeneity of matrix properties and for example randomly distributed fracture angles (Watanabe network) and/or heterogeneous fracture apertures (Watanabe and Sierpinski network). Our work is connected to uncertainty in site characterization [Ezzedine, 2010] with Monte Carlo simulations.

We presented computationally efficient quantitative forecasting of site-specific geothermal energy extraction simulations of heat transfer between two boreholes. The hydraulic regime is the key determinant in the computational efficiency of the method and its translation into a velocity field, determined by the conceptualization of the chosen network, is to critical on geothermal performance.

ACKNOWLEDGEMENTS

The text of this chapter contains reprint of the material as it appears in the publication “Efficient simulations of heat transfer in fractured rocks” in the PROCEEDINGS, 43rd Workshop on Geothermal Reservoir Engineering, 2018. Gisladdottir, V., Roubinet D., Tartakovsky D.. The dissertation author was the primary investigator and author of this article.

Chapter 4

Lagrangian simulations of heat transfer in fractured rocks

4.1 Introduction

Modeling heat transport in fractured porous media is of importance in many applications. The structural properties of ambient rocks can be impacted by heat conduction as it can modify rock alteration patterns [Xu and Pruess, 2001] as well as reopen or create new microfractures [Wang et al., 1989; Lin, 2002]. In some cases heat variations in fractured medium can cause seismic activity when performing enhanced geothermal energy harvesting [Gunasekera et al., 2003; Chen and Shearer, 2011]. In enhanced oil harvesting heat transfer is of importance since oil viscosity can be reduced by injecting hot water or steam, to increase the rock temperature [Al-Hadhrami and Blunt, 2001]. For nuclear waste management, it is of importance to prevent leakage due to heat generated by radioactive decay [Xiang and Zhang, 2012; Wang et al., 1981].

Although heat transport in fractured porous media is of importance in many applications, one particular application is geothermal energy production. The harvesting process requires extracting geothermal fluid from a reservoir through boreholes. After the heat has been extracted

from the fluid the fluid is re-injected into the reservoir now at a lower temperature. The re-injection is critical to maintaining the performance of the reservoir as it maintains its pressure. Additionally, it minimizes the environmental impact of the production as it prevents onsite lagoon formations. Although the re-injection boreholes are vital, they run the risk of introducing cooler fluid to a production site and thus causing performance drop. It is therefore critical to having a thorough understanding of the interplay between the production and the re-injection boreholes when designing and engineering the locations of such boreholes. This interplay can be modeled as a heat transfer in fractured porous medium using our method.

The complexity of simulating heat transfer in fractured porous media is due to the stark contrast between thermal and hydraulic properties in the advective fluid-filled fractures, the conduction in the ambient matrix (heat storage medium) [Bruel, 2002, Kolditz, 1995], as well as capturing the heat exchange between the two domains [Carrera et al., 1998, Neretnieks, 1983]. Additionally, the spatial extent of the exchange area is dependent on the topography, whose multi-scale nature of fracture lengths (meter-scale) and aperture (millimeter-scale) adds another layer of complexity [Bonnet et al., 2001, Bour and Davy, 1999, Neuman, 2005]. Determining the topology and the heat transfer across it directly determines the reservoirs heat extraction potential.

To do the transport processes justice the models have to account for the presence of fractures (with different hierarchy of scales). The representative elementary volume might not apply to such fractured media, rendering standard homogenization [Long et al., 1982, Painter and Cvetkovic, 2005, Roubinet et al., 2010a] or single-continuum advection-dispersion equation(ADE) models infeasible. To address this problem in solute transport, two frameworks have been proposed. In one of the frameworks, the fractured rock is treated as a stochastic continuum with random field transport properties. Either the assumption is made that there is a scale where the stochastic-advection-dispersion equation (SADE) is valid [Neuman, 2005] or that there is no such scale and therefore using other methods e.g. particle methods continuous

time random walk models [Berkowitz and Scher, 1997]. The other framework, discrete fracture network (DFN), does not assume continuum but instead accounts for dominant fractures. While the DFN framework is able to capture the multi-scale phenomenon (millimeter aperture for fractures in multi meter domains fractures) involved in modeling dominant fractures and the the distinct flows and thermal properties, it can also be prohibitively computationally heavy [Karra et al., 2018]. Both deterministic [Dverstorp et al., 1992, ?] and stochastic [Cacas et al., 1990, Ezzedine, 2010] fracture networks have been used in DFN models.

The requirements of numerical schemes with multi-scale meshing render these models computationally prohibitive even for methods using nonuniform meshes. A simulation of a uniform mesh for the same governing equations, boundary, and initial conditions, without a super computer would require a drastic simplification. On the other hand non-uniform mesh, although computationally more efficient, often requires manual adjustment with each alteration of the fracture network. Our results show that the particle method presented in this paper produces substantial results/insight with dramatically reduced computational complexity, while capturing the multi-scale geometry of physical processes found in nature for a variety of network.

The CPU efficiency of such particle methods is the motivation for the development of mesh-free particle based solvers for transport in fracture [Painter et al., 2008], and in our previous work, mass and heat transport in fracture networks with one dimensional conduction in the matrix, [Roubinet et al., 2010b] and [Gisladdottir et al., 2016] respectively. Here we develop a more general approach that does not make this assumption. Instead in our enhanced approach accounts for both transversal and longitudinal, two dimensional, conduction in the ambient matrix for heat transfer, while achieving substantially improved computational efficiency. We are not aware of a similar method for 2D conduction in the matrix. Some of the literature makes the claim that one-dimensional conduction is sufficient for modeling purposes [?], where as other studies demonstrate that the two-dimensional conduction is an important mechanism in the modeling [Kolditz, 1995, Ruiz Martinez et al., 2014, ?]. Our results shows that in some

parametric regime the former does apply while in others the multi-dimensional conduction is required. The mesh-free numerical particle method that accounts for two dimensional conduction is presented in Section 4.3. In Section 4.4 shows numerical experiments with one- and two-dimensional conduction in the matrix heat transfer. Then in Section 4.5 the results from the simulations are interpreted and discussed.

4.2 Problem Formulation

For the purpose of studying heat transfer in fractured porous media, we consider the impact topography and the physical assumptions of conduction in the matrix on the heat transfer - specifically the implications of using multi-dimensional conduction as compared to one dimensional conduction. The Sierpinski lattices representing the fracture network are described in section 4.2.1, the fluid flow is introduced in 2.2.2, and the heat transfer processes with multi-dimensional conduction in the matrix are presented in section 4.2.2.

4.2.1 Fracture Network represented by Sierpinski lattices

The fractal geometry is found in geological structures as is seen in fracture networks who often have a hierarchical or fractal structure [Mandelbrot, 1982, ?]. Multiple fracture networks have been used for transport modeling. Sierpinski lattices are an example of synthetic fractal fracture patterns whose have been used to simulate dynamic processes in hierarchically fractured rocks [Doughty and Karasaki, 2002, Roubinet et al., 2013a]. In Sierpinski networks, domain is subdivided into nine equal squares by two orthogonal sets of fractures. For a domain of size of L , each fracture spacing, both between the fractures and the distance from the domain border, is $L/3$. This is referred to as the template. Then N_{sq} squares are filled with the template. When the length of the templates set of orthogonal fractures is $L/3$ (and the fracture spacing is $L/3$), this is known as level 2. The process is then repeated until a desired level is reached. An example of a

level-3 Sierpinski lattice with $N_{sq} = 3$ and orthogonal fracture set with smallest fracture length equal to $L/3$ is shown in Figure 4.1.

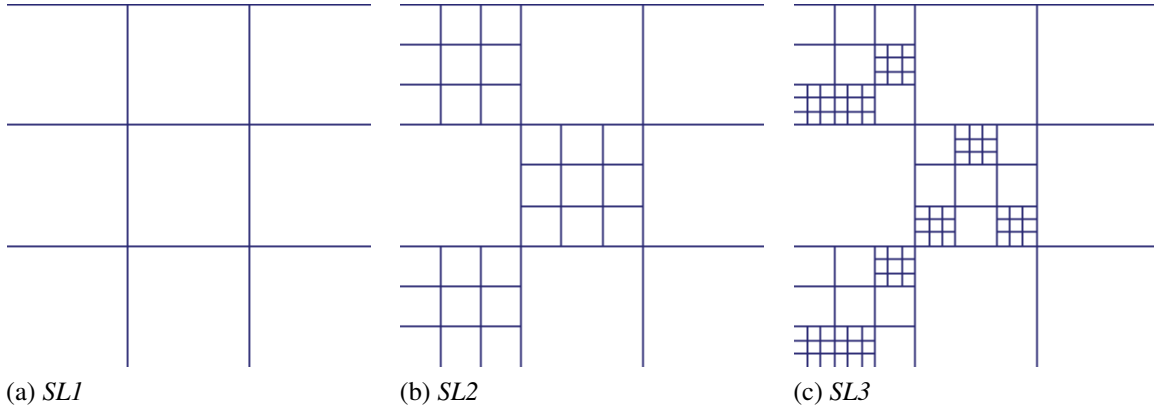


Figure 4.1: Sierpinski networks with levels 1, 2, and 3, respectively SL1, SL2, and SL3.

4.2.2 Heat transfer in fracture-matrix systems

The Particle method presented in section 4.3 offers a solution to the problem of heat transfer in fractured porous medium. It is derived from the solution of the problem of heat transfer in a single fracture with aperture b in a infinite matrix. The formulation of a single fracture in an infinite matrix is as follows. The matrix is represented by $\Omega_m = \{(x, z) : 0 \leq x < \infty, |z| \geq b/2\}$ and the fracture by $\Omega_f = \{(x, z) : 0 \leq x < \infty, |z| \leq b/2\}$. The advection-dispersion equation (ADE) for the fluid temperature in the fracture satisfies

$$\frac{\partial T^f}{\partial t} + u \frac{\partial T^f}{\partial x} = D_L^f \frac{\partial^2 T^f}{\partial x^2} + D_T^f \frac{\partial^2 T^f}{\partial z^2} + f, \quad (x, z) \in \Omega_f, \quad (4.1)$$

where the fluid velocity computed in Section 2.2.2 is u , the forcing term is defined as $f = T_0 u \delta(x) \mathcal{H}(t)$, and D_T^f and D_L^f are the transverse and longitudinal dispersion coefficients, respectively. The definition of the coefficients are as follows $D_T^f = \lambda_T^f / (\rho c) + E_T^f / (\rho c)$ and $D_L^f = \lambda_L^f / (\rho c) + E_L^f / (\rho c)$, where the fluids' heat capacity is c ; the transverse and longitudinal thermal conductivity coefficients are λ_T^f and λ_L^f , respectively; The transverse and longitudinal thermal dispersion coefficients are E_T^f and E_L^f , respectively [Yang and Yeh, 2009]. With an

ambient matrix impervious to flow, the diffusion equation (DE) governing the temperature in the matrix, $T^m(x, z, t)$, is

$$\frac{\partial T^m}{\partial t} = D_L^m \frac{\partial^2 T^m}{\partial x^2} + D_T^m \frac{\partial^2 T^m}{\partial z^2}, \quad (x, z) \in \Omega_m, \quad (4.2)$$

where D_T^m and D_L^m are the transverse and longitudinal dispersion coefficients, respectively. The definitions of the coefficients are as follows $D_L^m = \lambda_L^e / c_e$ and $D_T^m = \lambda_T^e / c_e$, the effective heat capacity of the matrix is c_e ; and the transverse and longitudinal thermal conductivity coefficients in the matrix are λ_T^e and λ_L^e , respectively.

The continuity of heat and temperature is ensured with the following conditions at the fracture-matrix interfaces

$$T^f = T^m, \quad \phi_m D_T^m \frac{\partial T^m}{\partial z} = D_T^f \frac{\partial T^f}{\partial z} \quad (4.3)$$

where c_s and ρ_s are the heat capacity and density of the solid phase, respectively; the matrix porosity is ϕ ; and $\phi_m = [\phi + (1 - \phi)\rho_s c_s / (\rho c)]$. and equations (4.1) and (4.2) have the following initial conditions

$$T^f(x, z, 0) = T_i(x, z), \quad T^m(x, z, 0) = T_i(x, z) \quad (4.4)$$

and boundary conditions

$$T^f(\pm\infty, z, t) = T_i, \quad \frac{\partial T^f}{\partial z}(x, 0, t) = 0 \quad T^m(\pm\infty, z, t) = T_i, \quad T^m(x, \infty, t) = T_i \quad (4.5)$$

4.3 Particle method for heat transfer in fractured media with two dimensional diffusion in the matrix

In previous work, we presented Lagrangian simulation using a particle method for heat transport in fracture media with one dimensional conduction in the matrix, [Gisladottir et al., 2016]. Here we expand on that method by presenting a particle method with multi-dimensional conduction in the matrix.

The method takes place at three scales: the fracture-matrix scale where the heat transfer is captured by conduction in the infinite matrix and advection in the fracture (Section 4.3.1); the matrix-block scale, where heat conduction is restricted because particles might transfer to neighboring fractures (Section 4.3.2- 4.3.2); and the fracture network scale, heat flux conservation is ensured by probabilistically determining which fracture enters using the flow rate distribution and intersection configuration (Section 4.3.2).

4.3.1 Probabilistic expression of temperature in single fractures

For the fracture-matrix scale, we use the boundary-value problem (4.1)–(4.5), which is simplified to lend it self to a closed form solution [Ruiz Martinez et al., 2014]. For fluid temperature in the fracture with constant injection, the ADE with multidimensional conduction has an analytical solution given by

$$T^f(x, t) = \frac{1}{2R_0} \left[\operatorname{sgn}(x) - \frac{R}{\pi} \operatorname{Ei} \left(-\frac{1}{4t_{\text{diff}}^*} \right) - \operatorname{erf} \left(\frac{R}{2\sqrt{R_0 t_{\text{diff}}^*}} \right) \right] + \frac{R_1}{2R_0^{2/3} t_a^* \pi} \exp \left(-\frac{R^2}{4R_0 t_{\text{diff}}^*} \right) \left(\frac{2t_a^*}{R_1} - \frac{\sqrt{t_{\text{diff}}^* \pi}}{RR_0} - \frac{1}{R_0^2} \right) \quad (4.6)$$

where $R = (\phi \sqrt{D_T D_L}) / (ub)$, $R_0 = R^2 + 1$ and $R_1 = R^4 + R^2 + 2$. We observe the fluid temperature at an observation point $x = L$, for a finite observation time t_{max} . Let $T_{\text{max}} = \max\{T(t; x = L) :$

$0 \leq t \leq t_{\max}$ }, the maximum temperature reached there during the observation time. Then using (4.6), at $x = L$, and normalizing with T_{\max} we determine the cumulative distribution function for the fluid temperature at time t to be represented by

$$T_c(t; x = L) = \frac{T^f(t; x = L)}{T_{\max}}, \quad t \in (0 \quad t_{\max}) \quad (4.7)$$

T_c is a continuous function which is monotonically increasing on the domain $[0 \ 1]$ hence fulfilling the properties of a CDF. Thus the CDF representing fluid temperature at a given point in space, L , is treated

$$T_c(t; L) = P(\tau < t) \quad (4.8)$$

resulting in the probabilistic cumulative distribution of the relative temperature as a function of time.

However, our goal is to understand the heat propagation, and thus the distribution of how heat traverse through the system. The CDF of the heat distribution $T_c(t; L)$ effectively describes the number concentration of particles having arrived at L at time t . We are interested in the probabilistic distribution of the diffusion time, i.e. the time that it takes a certain heat particle to arrive to L . For this purpose equation 4.8 is inverted. From this distribution the arrival time is drawn. We achieve this by replacing $P(t < \tau)$ with a uniform random variable $U \in [0, 1]$, and the function is then evaluated for t using a global Newton-Raphson method.

4.3.2 Accounting for the presence of neighboring fractures

For the transport in the network the effects of the neighboring fractures need to be taken into account (i.e. the finite size of the matrix blocks). This is done by first segmenting the fracture and identify the time it takes a particle to cross each segment (section 4.3.2), and then using that information by determining weather the particle crosses the segment (remains in the fracture) or transfers to a neighboring fracture using a particle transfer process described in section 4.3.2.

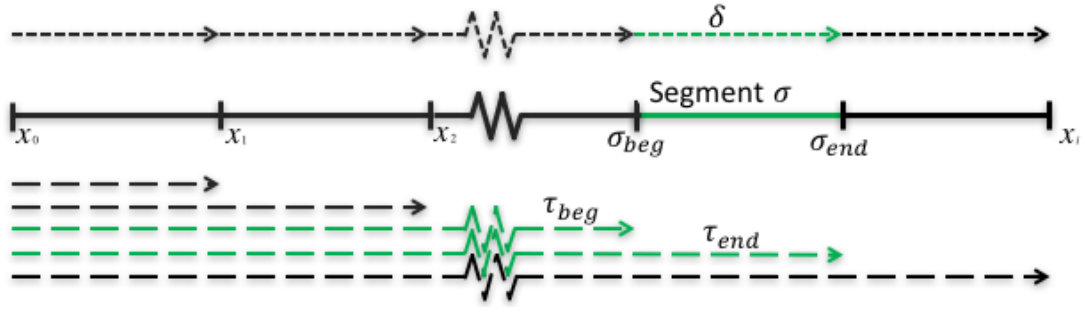


Figure 4.2: Segmenting the fracture

Segmenting the fracture

We consider a segment, σ , of the fracture with length $L_\sigma = \sigma_{end} - \sigma_{beg}$. The time it takes to transverse segment σ is a random variable δ described by corresponding cumulative distribution function (CDF). The distribution for the time it takes to travel from the origin of the fracture to the beginning of the segment, τ_{beg} , is represented by $T_c(t; L = \sigma_{beg})$. Similarly the distribution for the time it takes to travel from the origin of the fracture to the end of the segment τ_{end} is the $T_c(t; L = \sigma_{end})$. It follows, that

$$\tau_{end} = \delta + \tau_{beg} \quad (4.9)$$

Moreover, we observe that δ and τ_{beg} are independent random variables. It follows that cumulative distribution function for τ_{end} is equal to the convolution of the cumulative distribution function of τ_{beg} and the probability density function of δ , or [Miller, 2017]:

$$T_c(s; \sigma_{end}) = \int_0^\infty T_c(s-t; \sigma_{beg}) f^\delta(t) dt \quad (4.10)$$

where $f^\delta(t)$ is the PDF for δ .

Unfortunately 4.10 does not lend itself to a closed form solution for $f^\delta(t)$. However, we can

derive $f^\delta(t)$ numerically as follows.

First, by discretizing the timeline into time increments δ , we define the discrete sequence $\{c_i : c_i = T_c(i\Delta t; \sigma_{\text{end}})\}$. Full definition of CDF i.e. $P(t \leq idt)$. It follows that this sequence defines a discrete CDF T'_c corresponding to the continuous CDF of T_c . Further define the sequence $\{e_i : a_0 = c_0; e_i = c_i - c_{i-1} \forall i > 0\}$. It follows that the sequence e_i , defines the discrete PMF, corresponding the CDF at σ_{end} . We similarly define the PMF corresponding to the CDF at σ_{end} , by the sequence $\{b_i, i \geq 0\}$, using $T(i\delta t; \sigma_{\text{begin}})$. For any discrete random variable X values in the non-negative integers $\{0, 1, \dots\}$, then the probability generating function of X is defined as [Miller, 2017]

$$G(z) = E(z^X) = \sum_{x=0}^{\infty} p(x)z^x, \quad (4.11)$$

where p is the probability mass function of X . The power series converges absolutely at least for all complex numbers z with $|z| \leq 1$.

From this, and using the sequences above we obtain the probability generating functions

$$G_{\text{end}}(s) = \sum_{i=0}^{\infty} a_i s^i \quad G_{\text{beg}}(s) = \sum_{i=0}^{\infty} b_i s^i \quad G_{\delta}(s) = \sum_{i=0}^{\infty} D_i s^i \quad (4.12)$$

Then it follows that G_{beg} is the probability generating function for the discrete distribution corresponding to $T(i\delta t; \sigma_{\text{begin}})$. Similarly, G_{end} , is the probability generating function for the discrete distribution corresponding to $T(i\delta t; \sigma_{\text{end}})$. By reducing δt to smaller and smaller values, we can make the correspondence arbitrarily close to the continuous version of the distribution. Lastly we define G_{δ} as the generating function for the values of δ and D is δ 's probability mass function. Our goal is to solve As before, since t_{beg} and delta are independent, their sum is given by the convolution of their respective generating functions, giving us [Miller, 2017]

$$G_{\text{end}}(s) = G_{\text{beg}}(s)G_{\delta}(s) \quad (4.13)$$

We seek to calculate the coefficients of $G_\delta(s)$, effectively inverting the convolution. By matching the corresponding powers of s on each side this is relatively straight forward (assuming b_0 is not 0 for that special case), and we get: [Miller, 2017]

$$\{a_k : a_k = \sum_{l=0}^k b_l D_{k-l}\} \quad (4.14)$$

This is the equivalent of a lower diagonal triangle matrix and can be calculate iteratively. We therefore obtain:

$$\{D_k : D_0 = \frac{a_0}{b_0}; D_k = \frac{1}{b_0} \left(a_k - \sum_{l=1}^k b_l D_{k-l} \right) \quad \forall \quad k > 0\} \quad (4.15)$$

and its corresponding numerical cumulative distribution for δ as

$$\{h_i : h_0 = D_0; h_i = D_i + h_{i-1} \forall i > 0\} \quad (4.16)$$

Using this discrete cumulative distribution of the relative temperature of the segment σ we use equation 4.8 to determine the time for heat propagation across the segment σ .

$$T_\delta(t) = P(t < \tau) \quad (4.17)$$

providing a probabilistic cumulative distribution of the relative temperature in segment σ as a function of time.

To randomly draw the arrival times of the particles from this distribution $P(t < \tau)$ is replaced with U a uniform random generator, where $U \in [0, 1]$. Since T_δ has a numerical representation (see Equation 4.16) the function is evaluated with a numerical approach, by identify the value in $\{h\}$ that U corresponds with or the interval in $\{h\}$ that it lives on. In the former case the index on $\{h\}$ provides the index in the time vector that is our diffusion time. In

the later case, extrapolation provide the t_δ .

Using this approach does introduce an error for $f_\delta(t)$ at very small t due to a numerical instability at the boundary in $f_{\text{end}}(t)$ and $f_{\text{beg}}(t)$ to address that the first element of the PMF vectors is evaluated for the functions is evaluated at a slightly larger time value then t_0 . This avoids the instability and the margin of error that it introduces in the mass of the probability mass function ranges from 10^{-6} to 10^{-2} depending the fracture and hydraulic properties. Additionally, the analytical solution (see Equation 4.6) only holds true for $t > t_{\text{min}}$ and therefore for values smaller then that one dimensional conduction is assumed in the matrix and the heat transfer approach from our previous work [Gisladottir et al., 2016] is applied.

Particle transfer

The effects of a neighboring fracture are incorporated with particle transfer. For this purpose we consider the case where there are three parallel fractures where one is located at l_i , fracture of origin, another above, f_1 located at l_1 , and fracture below, f_2 located at l_2 . Noting that the distance between the fracture of origin and the fracture above ($|l_i - l_1|$) does not have to be equal to the distance between fracture of origin and the fracture below ($|l_i - l_2|$). Each particle that conducts into the matrix, leaving the fracture of origin, has the probability of reaching fracture f_1 without crossing fracture f_2 , P_{transfer}^1 . The same applies for its probability of reaching fracture f_2 without crossing fracture f_1 , P_{transfer}^2 . In La place domain these probabilities are defined as [Feller, 1954]

$$\bar{P}_{\text{transfer}}^1 = \frac{\exp(l_1 \sqrt{s/D_T^m})}{s} \frac{1 - \exp(-2l_2 \sqrt{s/D_T^m})}{1 - \exp[2(l_1 - l_2) \sqrt{s/D_T^m}]} \quad (4.18a)$$

$$\bar{P}_{\text{transfer}}^2 = \frac{\exp(l_2 \sqrt{s/D_T^m})}{s} \frac{1 - \exp(-2l_1 \sqrt{s/D_T^m})}{1 - \exp[2(l_2 - l_1) \sqrt{s/D_T^m}]}, \quad (4.18b)$$

where s is the Laplace variable. These expressions numerical inversion is found using the method from [Stehfest, 1970]

This solution, of first passage time, assumes 1D conduction in the matrix. First passage time for when a particle escapes a strip of parallel barrier is the same for Brownian motion with 1D conduction and 2D conduction. If there are particles traveling in a domain with three parallel fractures at $y = 0$, $y = l_1$ and $y = l_2$ (see Figure 4.3). The transport across the 2D domain is composed of two components $(C_L(t), B_T(t))$. The first component represents the transport in the longitudinal direction and the second the transport in the transverse direction. The transverse transport is governed by Brownian motion and the particles are released into the system from the fracture at $y = 0$ into the system. They can reach fractures located at $y = l_1$ or $y = l_2$ in which case they are absorbed. We are interested in the First Passage Time of the particles reaching those fractures. Since the second component of the process is not influenced by the first component (i.e. the second process is independent of where it is located in the x).

$$T = \inf\{t \geq 0 : B_T(t) = l_1 \quad \text{or} \quad l_2\} \quad (4.19)$$

Therefore, the solution for First Passage Time with 1D conduction introduced by Feller in 1954 will provide the time it took a particle to conduct through the matrix between two parallel plates with two dimensional conduction (Prof. Williams, communication). Although the assumption is made here that the particle enters the neighboring fracture at a point perpendicular to where it left the fracture of origin. The time that a particle takes conducting in the matrix and where it travels two are determined in the following way. First we identify the the probability for a particle to transfer to a neighboring fracture, P_{transfer} , and its corresponding transfer time, t_{transfer} smaller than the maximum conduction time t_c^∞ , as follows

$$P_{\text{transfer}} = P_{\text{transfer}}^1 (t_{\text{transfer}} \leq t_c^\infty) + P_{\text{transfer}}^2 (t_{\text{transfer}} \leq t_c^\infty). \quad (4.20)$$

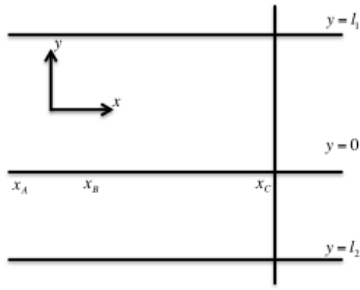


Figure 4.3: Three parallel fractures. The particles originate from the fracture at $y = 0$ and can diffuse to fractures located at $y = l_1$ or $y = l_2$ where they are absorbed.

Next a random number U is drawn from a uniform distribution of the interval $[0, 1]$. IF $U < P_{\text{transfer}}$ the particle is assumed to transfer and the value is used to determine transfer time by solving $P_{\text{transfer}}(t \leq t_{\text{transfer}}) = U$. Otherwise the particle does not transfer and is consider to return to its fracture of origin displaying behavior of a single fracture in an infinite matrix which is therefore used to calculate the conduction time, t_c^∞ , to cross a set distance of the segment of the fracture. If a particle transfer takes place, the particl transfers to fracture f_1 if

$$\frac{U}{U_{\max}} > \frac{l_1}{l_1 + l_2} \quad (4.21)$$

holds true. Otherwise it transfers to f_2 with $U_{\max} = P_{\text{transfer}}$. If a particle crosses the entire length of the fracture, with out transferring to a neighboring fracture during its time in the matrix, it reaches an intersection which forks into multiple fractures. The fracture that the particle enters at the intersection is based on the configuration of the intersection and the flow rate distribution. The particle can only enter a fracture whose flow is leaving the intersection (i.e. positive velocity) and complete mixing and streamline routing rules are assumed [Hull and Koslow, 1986, Berkowitz et al., 1994]. The probability of a particle entering a fracture with a positive velocity is based on the flow rate ratio between the fractures that have a potential of being entered. In the special case when a particle can enter into two fractures, then if the closest fracture has a dominant flow rate the particle has a priority of enter set fracture [Le Goc, 2009a].

4.4 Simulations

4.4.1 Heat transfer simulations

To study the heat transfer we consider a square domain of length $L = 0.5$ m across which there is an interconnected fracture network in the form of Sierpinski lattices. For the Sierpinski networks, the $N_{sq} = 3$ and the simulations are performed on Sierpinski networks with levels 1, 2, and 3, which is presented in Figure 4.1. The flow across the network is assumed to enter the fractures intersecting the left side of the domain and exit through the fracture on the right hand side of the domain. To study different hydraulic regimes two different heat gradients are applied. The hydraulic regime i) applies a gradient of $2.3 \cdot 10^{-3}$ and hydraulic regime ii) is one order magnitude smaller or $2.3 \cdot 10^{-4}$. For the top and bottom boundary no-flow conditions are assumed and the flow travels through the interconnected network. The flow velocity fields are calculated using a fluid density $\rho = 10^3$ kg/m³ and dynamic viscosity $\mu = 10^{-3}$ kg/(m·s).

The Lagrangian heat transfer simulation is performed on the interconnected fracture networks presented in Figure 4.1 where the domain is considered to be in an infinite matrix. For each of the fracture network and each flow regime two heat transfer process are simulated where the particles are injected into the fractures intersecting the left hand side of the domain and then transferred across the domain until they reach the right hand side. The first heat transfer process transports the particles across the domain according to the particle method presented in Section 4.3.2. In for comparison the latter assumes that there is no transfer between the fractures (i.e. each fracture is treated as it is in an infinite domain). The thermal arrival is recorded. The rock porosity is $\phi = 0.78$. Thermal parameters are provided in Table 2.2.

In Figures 4.5-4.6 we look at the relative temperature curves for heat transfer across the interconnected networks S1, S2, and S3, with hydraulic regime i) with one-dimensional and two dimensional conduction in the matrix, respectively. Here the relative temperature T^* is defined

as

$$T^* = \frac{T_{\text{ext}} - T_0}{T_{\text{inj}} - T_0} \quad (4.22)$$

the temperature of the fluid at the right side of the domain, representing the the extraction site, is T_{ext} , and the temperature of the fluid at the left side of the domain with continuous injection is T_{inj} . These curves are obtained from the cumulative distribution functions (CDFs) of the particle arrival times using $N = 5000$ particles, and these results are similar to those obtained from 10^4 particles.

4.5 Results

4.5.1 Comparison

To demonstrate the effectiveness of our particle transport across segmented fracture approach in section 4.3.2 we compare it against the analytical solution for a single fracture in an infinite matrix found in equation (4.6). Lets consider the case of a fracture of length $L = 0.5$ m in an infinite domain. The fracture is segmented into two parts. A particles crosses the first segment using equations (4.6)–(4.8) to determine the conduction time t_c . The conduction time for the second segment is determined using the approach presented in Section 4.3.2. This is done for 5000 particles and the temperature profile it produces is plotted (green circles) against the analytical solution (red line) in Figure 4.4. Our result demonstrate that the probabilistic method captures the ADE behavior of the analytical solutions.

4.5.2 Heat transfer in fracture networks

We look at the heat transfer across Sierpinski fracture networks level 1, 2, and 3, known as SL1, SL2, and SL3 respectively (see Figure 4.1). In Figure 4.5 we have temperature as a

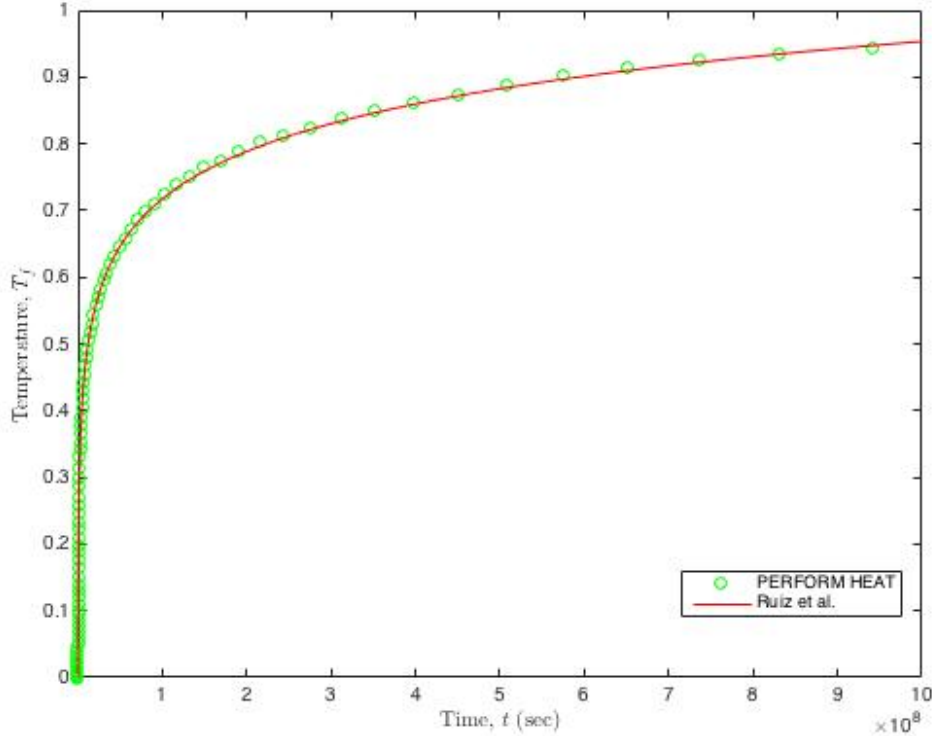


Figure 4.4: The temperature at the end of the fracture as a function of time computed with the analytical solution by Ruiz et. al 2012 treating the fracture as single segment (red solid line) and with the particle method and probabilistic generating functions where the fracture is made up of two segments (green circles).

function of time for the particle method we presented in [Gisladdottir et al., 2016]. The thermal breakthrough for the SL1 network is slower than the ones for SL2 and SL3. The 50% performance drop for SL3 is slightly above 10^5 whereas for SL1 it is closer to $5 \cdot 10^5$. In Figure 4.6 the same simulation is performed using the extended Lagrangian particle method presented in this paper with multi-dimensional conduction in the matrix. With the multi-dimensional conduction in the matrix SL2 and SL3 exhibit a slower thermal breakthrough whereas SL1 thermal breakthrough is earlier. The same reversal of behavior is observed for 50% performance drop. For the later simulation the SL1 takes place before the SL2 and SL3. In this case the performance drop in SL1 is half an order of magnitude faster than simulation with the initial method i.e. occurs at 10^5 , whereas the 50% performance drop is quite similar to that in SL3.

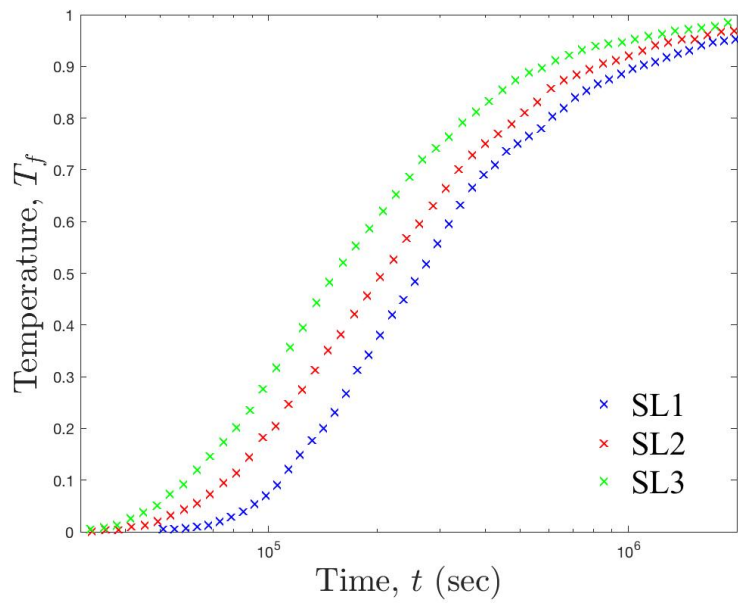


Figure 4.5: Sierpinski level 1,2, and 3 with one dimensional conduction in the matrix.

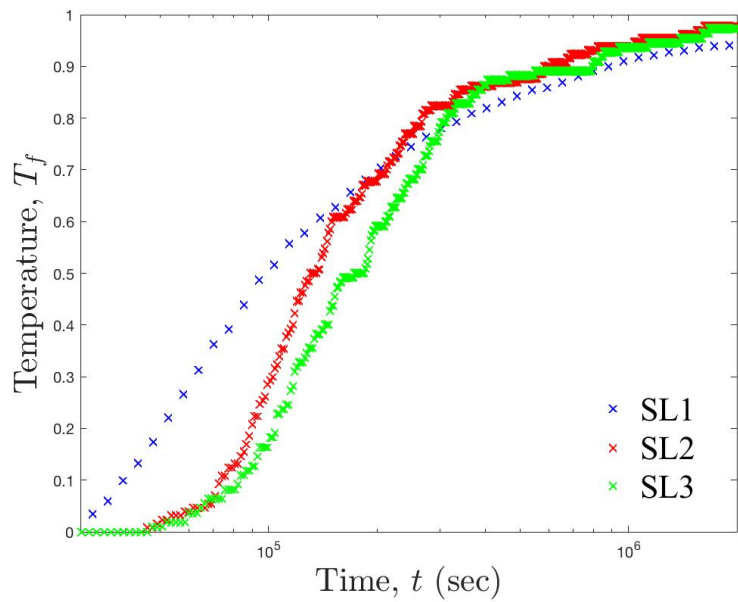


Figure 4.6: Sierpinski level 1,2, and 3 with two dimensional conduction in the matrix.

4.6 Conclusion

Quantitative understanding of heat transfer processes in fractured porous media is critical for effective geothermal energy harvesting. We have presented a novel mesh-free heat transfer Lagrangian particle-tracking approach to model this interaction. Our approach allows us to model more realistic discrete fracture networks, while achieving computational efficiency that significantly exceeds that of standard (mesh-based) numerical methods. Our approach has the ability to account for multi-dimensional conduction in the matrix enabling us to study the effects of conduction dimensionality on the model. Some of the literature makes the claim that one-dimensional conduction is sufficient for modeling purposes [?], whereas other studies demonstrate that the two-dimensional conduction is an important mechanism in the modeling (Kolditz 1995 [?]). Our results show that for the parameter set studies that for simpler networks dimension of the conduction in the matrix can have an impact on the performance drop of the system whereas for the more complex networks the difference is less. The fact that the particle can only re-enter the fracture of origin at the point it exited the fracture (i.e. with one-dimension conduction in the matrix) rather than having the possibility of reentering the fracture downstream has more impact on the simpler networks. In those networks when a particle enters the matrix the particles are more likely to reenter the fracture of origin rather than to diffuse to a neighboring fracture.

Although the low-computational cost of our method is attractive, some improvements could be introduced in future studies. These include incorporation of heterogeneity of matrix properties, study the potential effects of the dimensionality of the conduction in the matrix in different parameter settings, and extensions to three-dimensional conditions.

ACKNOWLEDGEMENTS

The text of this chapter contains reprint of the material as it appears in the publication “Lagrangian simulations of heat transfer in fractured rocks”, (in preparation for submission). Gisladdottir, V., Roubinet D., Tartakovsky D.. The dissertation author was the primary investigator and author of this article.

Chapter 5

Resilience of cyber systems with over- and under- regulation

5.1 Introduction

National Institute of Standards and Technology, Department of Homeland Security, and other agencies are applying traditional risk assessment paradigms to cyber security [Sedgewick, 2014],[Nat, 2014]. The objective of cyber security is to protect the hardware, software, and information on computer systems against specific Threats (e.g., adversaries) that are trying to exploit system Vulnerabilities (e.g., web browsing) to achieve Consequences that would result in either economic or political impacts. Most efforts in cyber security are focused on decreasing system vulnerabilities and, to a lesser extent, the consequences of a successful attack (e.g., by creating backups of important data). In addition to fixes in software and hardware design, the introduction of operational constraints through the use of rules is a widely applied risk management practice in a number of fields [Shleifer, 2005, A., 2005] . Rules are designed to limit operator access to certain components of the system and decrease their ability to intentionally or unintentionally create new vulnerabilities. However, rules can negatively impact cyber security

due to human factors. Cyber security is typically studied from a computer science perspective and traditional approaches often do not incorporate behavioral science. As Douglas Maughan, head of cyber security research at the U.S. Department of Homeland Security, describes, "We've had too many computer scientists looking at cybersecurity, and not enough psychologists, economists and human-factors people" [Waldrop, 2016]. Under-regulation in systems with high vulnerability opens these systems to outside attacks. Rules play a key role in implementing and enforcing security objectives, i.e., preventing a breach or aiding recovering after an adverse event. Rules provide a means for ensuring that employees have access to relevant information to maintain system functionality and to minimize the access to sensitive components of the system. Because under-regulation often leads to system collapse and creates opportunity for disruptions [USGPO, 2015, Gunningham and Johnstone, 1999], rules are required to establish barriers to external threats. Even though stricter regulation decreases risk related to external threats, it can also increase risk due to human factors associated with the rules' implementation (e.g., demanding regular password changes (8). As regulations become too restrictive, impeding people's ability to perform their jobs, people inevitably start to circumvent or outright disregard these regulations. Hence, in practice, the regulations might as well not exist [A., 2005, Kepner et al., 2015, Magat et al., 1988]. Additionally, as the number of rules exceeds a certain threshold, people are more likely to make mistakes and be less motivated to follow the rules (11-13). Most people's objective isn't to stay secure, but to get their job done [Waldrop, 2016]. A reasonable inference, therefore, is that increased rules transfer risk from external threats to internal vulnerabilities, there is some intermediate number of rules that minimizes the overall risk level (Figure 5.1). But unless we have some idea where that point is, this Goldilocks observation is not of much use.

Neither is risk the whole story when it comes to ensuring system function. Notably, over-regulation may decrease a system's resilience with respect to insider threats. Resilience, as defined by the National Academy of Science, is the ability of a system to absorb, recover and adapt to both known and unknown threats [Council et al., 2012]. Over-regulation may increase



Figure 5.1: System risk is a function of the number of rules. The red line represents the risk from external threats; the blue line represents the risk from internal vulnerabilities; and the green line represents the combined risk from external threats and internal vulnerabilities.

the time that a system needs to recover from a cyber-attack, thus reducing its resilience [Zhu and Başar, 2011]. This is especially true if the attack is focused on human-related vulnerabilities. It has been observed that a significant increase in the number of rules imposed upon a complex technological system (e.g. railways and nuclear power plants) can cause rules to lose effectiveness [Aizenman, 2009]. Analyzing a system’s resilience is an effective way to understand the relationship between the risk management strategies regulating the system and its functionality. Risk assessment starts with the development of a threat scenario (often hypothetical), whereas resilience assessment starts with the definition of the system’s critical functions and their temporal patterns. Rules acting on specific system vulnerabilities, as opposed to the collective effect on the system’s performance, may merely provide incremental protection at the component level [Shleifer, 2005, Waldrop, 2016] and cause the temporal nature of resilience to be ignored [Linkov et al., 2014]. Even though the influence of over- and under-regulation on the system’s performance has been widely discussed in the academic literature and there is a significant number of studies on how to change people’s habits, the reports on quantitative modeling that incorporate both are lacking. Specifically, rule-risk models have been developed for analyzing individual behavior (e.g., Kepner et al. [2015]), and in various ways, resilience in organizations has been analyzed using network models. Our point of departure is to extend the individual

rule-risk models by embedding them within a network model. Associated with such a model are various simple assumptions about the mechanisms through which individuals act and risks propagate. Such models are a useful step in building knowledge about phenomena such as the rules-risk-resilience relationship. System behaviors predicted by such models can be viewed as testable hypotheses whose assumptions may be refined to better reflect observed reality. To the extent that the model and any future refinements are valid, the model will also have prescriptive use for determining optimal rules, i.e., for operationalizing the general qualitative insight that there can be too few and too many rules. Thus, our short term questions to be answered by constructing this model are (1) does a simple mechanistic model produce the hypothesized rules-risk relationships and (2) in what range is the right number of rules? We construct a numerical example which serves as an experiment to inform answers to these questions. This is a step toward answering the related questions for much richer systems. We develop a model, to be formally defined in the next section, which represents an organization as a network of individual employees affected by cyber threats. The employees within the organization are connected according to their business relationships. Each of these employees also has to follow a certain number of rules, which is a simplified representation of human behavior. An initial attack on the system results in the delivery of a virus to one employee's computer. Depending on the employee's job functions, they may unintentionally propagate the virus to their collaborators. It is assumed that employees who cannot perform their work while upholding the rules will disregard the rules. This impacts the system's behavior and the size of the impact varies depending on the setup of the system. The results from this simple model will show that the pattern in Figure 5.1 is indeed an emergent system behavior: adding more rules increases the resilience of the system until it reaches a tipping point where the trend reverses indicating increased vulnerability in the system and increased risk.

5.2 Model and example

Here, we lay out the model and construct a numerical example which demonstrates the influence of rules on the resilience of an organization with respect to the diffusion of a threat across its business relationships network. In this network the nodes represent the employees of the organization, while the links show collaborations between these employees on various projects. The main acronyms, parameters (including their values used in the case study) and variables of the model are given in Table 5.1.

Table 5.1: Main acronyms, parameters, and variables of the model.

| Name | Values | Description |
|---------------------------------|----------------------|--|
| Mainacronyms | | |
| DL | | Users' decision latitude |
| CF | | Critical functionality of the network |
| R | | Resilience of the network |
| Parameters and variables | | |
| b | 1...50 | Number of rules (barriers placed on the unit segment) |
| K | | Critical functionality of the system |
| k | | Degree of a node in the network model |
| k_j | | Degree of node j in the network model |
| L_i | | Amount of D_L between barriers i and $i - 1$ |
| L_{\min} | 0.2, 0.25, 0.33, 0.5 | Minimal D_L required by users to perform normal activities in the 1D model |
| L_{\min}^k | | for a node of degree k in the network model |
| L_T | 0.5 | Amount of D_L required for a threat to succeed in an attack against a node |
| N | 10000 | Total number of nodes |
| N_{in} | | Number of infected nodes |
| N_{ns} | | Number of not-strict barriers the threat have to breach |
| N_s | | Number of strict barriers the threat have to breach |
| p_{det} | 0.01 | Probability that the user detects the threat at each time step |
| p_{new} | | Probability that the threat succeeds in an attack against a node |
| p_{ns} | 1 | Probability that the threat breaches a not-strict barrier |
| p_s | 0.1 | Probability that the threat breaches a strict barrier |
| T_C | 540 | Control time |
| T_{latency} | 10 | Threat latency time |
| V | | System vulnerability (same as L_{\min}) |

We assume that the modeled network is scale-free, that is, its degrees follow a power law. This assumption takes into account the heavy-tailed degree distribution often found in communication systems. To construct the network, we used a configuration algorithm [Catanzaro et al., 2005]. The algorithm starts with the generation of N power law distributed integers corresponding to the nodes' degrees, where N is the number of nodes in the network. Then, the links are placed between the nodes in accordance with these degrees. In this study the network consists of 10,000 nodes. The number of nodes was selected to be large enough to allow non-linear emergent effects to occur, while increasing the statistical fidelity of the simulations, and to be small enough to represent a significant fraction of real world businesses (according to the Census Bureau [USC, 2016] more than 30,000,000 people were working for firms of 10,000 or more employees in the U.S. in 2013). Barabasi et al. have shown ([Barabási and Albert, 1999]) that the World Wide Web degree distribution (as of 1999) follows the power law with the exponent of 2.1, while its average degree equals 5.46. We select the average degree to be 5, and the power law exponent of the degree distribution to be 2.25. The minimal degree of each node is 2 to exclude nodes that do not impact the virus diffusion process. These parameters unambiguously determine the maximal degree of a node as 88. The virus diffusion process starts when an insider (intentionally or unintentionally) sends an email with malicious code to their colleagues. The propagation of the virus throughout the network is dependent on the regulatory environments of the individual employees. We model the rules implemented within an organization as either strict or not-strict barriers. The strict barriers are defined as rules that are always followed by all employees, while the not-strict barriers represent the rules that may occasionally be circumvented. We assume, that an insider is able to cross any number of the non-strict barriers without raising red flags. Notably, if there are too many or too few rules the likelihood of an insider's success increases: while the presence of too few rules is not sufficient to prevent insiders from accomplishing their goals, the presence of too many rules causes users to disregard these rules (barriers) in order to perform their usual tasks, which renders the barriers

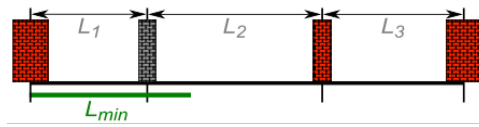


Figure 5.2: 1D users decision latitude model (9).

not-strict. These assumptions are intended to be rather non-controversial for inclusion in this investigation even though there could obviously be situations where they do not exactly hold.

5.2.1 Employees susceptibility to the virus

In order to evaluate a node's susceptibility to a threat, we use the concept of decision latitude (D_L) defined as the measure of the employee's ability to make work related decisions. Kepner et al(9) structurally represent the decision latitude as shown in Figure 5.2: they characterize the regulatory environment of a node as a set of barriers X_1, \dots, X_b placed on a unit segment of a straight line, where X_i is the position of the i th barrier. Then, the amount of decision latitude between barriers is defined as $L_i = X_i - X_{i-1}$. The sum of all the D_L amounts equals unity [Magat et al., 1988].

Similarly, we assign a unit segment of a possible rules implementation to the whole network, that is, each node (or each employee) has the same set of rules to follow. While in a real system there may be various levels of access and trust, in this initial approach they are ignored. The barriers' positions are drawn from a uniform distribution in the range (0; 1). It is easy to notice, that the modeled regulatory environment depends not only on the number of barriers (rules) but also on their stochastic placement. We account for this by running a set of 10,000 Monte-Carlo simulations for each data point. Let L_{min} denote the minimum value of decision latitude individuals need to perform their business tasks. In the original 1D model this value is a constant parameter. We assume that employees with more connections (higher node degree) have more expertise and therefore need less latitude to perform their work. To reflect this, we modify the 1D model so that the minimum latitude (L_{min}) depends on the node's degree and is



Figure 5.3: Model of the business relationships network (a) and its nodes' minimum decision latitudes (b). Notably, users of higher degrees have a smaller value of the decision latitude, a higher number of strict barriers (red) and, hence, are less vulnerable [Magat et al., 1988].

inversely proportional to the natural logarithm of that degree. Let k_j be the degree of node j . Then, presuming that the values of L_{\min} depend only on nodes' degrees (and not on any other topological parameters or properties of the network) we find the minimum latitude of all nodes with degree $k(L_{\min}^k)$ as follows (Figure 5.3):

$$L_{\min}^k = \frac{L_{\min}}{\ln k} N / \sum_{j=1}^N \frac{1}{\ln(k_j)} \quad (5.1)$$

Above, the multiplication by $N / \sum_{j=1}^N \frac{1}{\ln(k_j)}$ ensures that the average value of a node's minimum latitude across the whole network is L_{\min} . Notably, this formalism implies that the smallest degree in the network is 2. We now introduce the concept of strictness. Intuitively a barrier is strict if the employees execute their business functions on a regular basis without crossing the barrier. We define a barrier to be strict if $L_i > L_{\min}$ and not-strict otherwise.

Figure 5.3: Model of the business relationships network (a) and its nodes' minimum decision latitudes (b). Notably, users of higher degrees have a smaller value of the decision latitude, a higher number of strict barriers (red) and, hence, are less vulnerable.

Now we shift our attention to the idea that if a user is a nefarious insider they wish to execute a threat such as a virus. To represent the difficulty of executing the threat, we use L_T - the minimum latitude needed to execute the threat. The privileges most users need, and have, is less than what is needed to execute the threat, typically $L_T > L_{\min}$ (most users are restricted in access to sensitive corporate data). We presume that the adversary cannot control the set rules that must be exploited by the threat to successfully overcome the system's defense and model

that the threat latitude extends from 0 to L_T (as opposed to selecting the optimal for the adversary range on the unit segment). Therefore, we find the numbers of strict and not-strict barriers the adversary has to breach to succeed in attacking a node in the network, N_s and N_{ns} respectively, as the numbers of strict and not-strict barriers in the range $(0; L_T)$.

5.2.2 Infection propagating through the organization

An initial attack starts the process of propagating the threat through the network. For example, an infected email can spread a virus. The susceptibility of a new node, such as a user's station, becoming breached (or infected) is represented by the probability of breaching a new node in the network, which we derive as follows:

$$p_{\text{new}} = p_{\text{ns}}^{N_{\text{ns}}} p_{\text{s}}^{N_{\text{s}}} \quad (5.2)$$

Above, p_s is the probability for a threat to breach a strict barrier, and p_{ns} is the probability for a threat to breach a not strict barrier ($p_{ns} > p_s$). Once the probability of breaching a node is determined in the simulation, that value is compared to a randomly generated value $U: [0, 1]$. If $p_{\text{new}} > U$ the node is breached. When the breach of a new node in the network is successful, the threat needs latency time, T_{latency} , to collect information before attempting to breach neighboring nodes (e.g. sending email messages to collaborators of the person that just became infected). At every time step there is a probability that the user detects the threat (e.g. discovers a virus manually, or through antivirus check) which is represented by p_{det} . Once a threat is detected in a node, the node recovers and is considered to be immune to future breaches.

5.2.3 Resilience of the organization

Now that we have specified how threats propagate in a given system, we want to measure performance, i.e. the resilience of a system in face of threats. An organization's resilience is

its ability to prepare and plan, absorb, recover from, and more successfully adapt to adverse events(14). In this paper we model only the absorption and recovery phases of resilience according to the methodology proposed by Ganin et al. [2016] and evaluate the system's critical functionality (C_F), defined as the system's performance function of time, during the two aforementioned phases. For this simple case the critical functionality (K) is chosen as the ratio of uninfected nodes to the total number of nodes at each time step in the simulation. Let N_{in} be the number of infected nodes, then K is found as follows:

$$K = 1 - \frac{N_{in}}{N} \quad (5.3)$$

We assume that the preparation and adaptation phases of resilience do not take place during the attack, and therefore are not implemented in the simulation. Hence, we simulate the critical functionality of the system while it goes through the absorption and recovery phases. Those phases take place within control time T_C . The resilience value R is calculated by integrating the C_F over the time interval $[0, T_C]$ (21):

$$R = \frac{1}{T_c} \int_0^{T_c} K dt \quad (5.4)$$

The absorption phase starts directly after the initial attack when some nodes are breached while the others resist. The recovery phase occurs when the users detect the breach. Note that we model the system's evolution in discrete time steps, and therefore, equation 5.4 can be simplified to

$$R \approx 1 - \frac{1}{T_c} \sum_{t=0}^{T_c} \frac{N_{in}}{N} \quad (5.5)$$

5.3 Results

Figure 5.4 plots critical functionality as a function of time, and the risk and resilience as a function of number of rules. Each of the lines in figure 5.4b-c represents a different level of system vulnerability (V). We observe that at very high levels of vulnerability, risk is high and resilience is low regardless of regulations. Risk and resilience in highly vulnerable systems cannot be managed effectively, and as a result, vulnerability should be reduced first (this is what cybersecurity efforts are currently focused at). For lower (and thus more manageable) levels of vulnerability, we observe in each of the graphs that as the number of rules increase there is an initial decrease in risk down to a clear minimum, after which the trend reverses and risk steadily increases. The resilience exhibits a similar pattern, but in the opposite direction - there is clear optimality in the number of rules resulting in high system resilience. This indicates that the first few rules applied to the system decrease the risk and increase resilience. However, after reaching a tipping point the trend reverses, revealing that beyond a certain level additional rules may be detrimental. We note that in the numerical example, the peak value occurs at a relatively small number of rules (between 5 and 15), regardless of the level of vulnerability. Thus, this may be a reasonable range for system designers to consider in the absence of model assumptions and parameter values more explicitly customized for particular networks.

5.4 Conclusion

Administrators aim to find the optimal balance of regulation [Linkov et al., 2014] which decreases system risk and increases system resilience. While currently the malicious insider risks are assessed qualitatively with focus on the optimal number of employees (usually security guards) to maintain security [Carroll, 2004, Bunn, 2004, Sagan, 2004], Ghaffarzadegan [2008]), we call for a framework for a systematic evaluation of rules, risk, and resilience of cyber systems

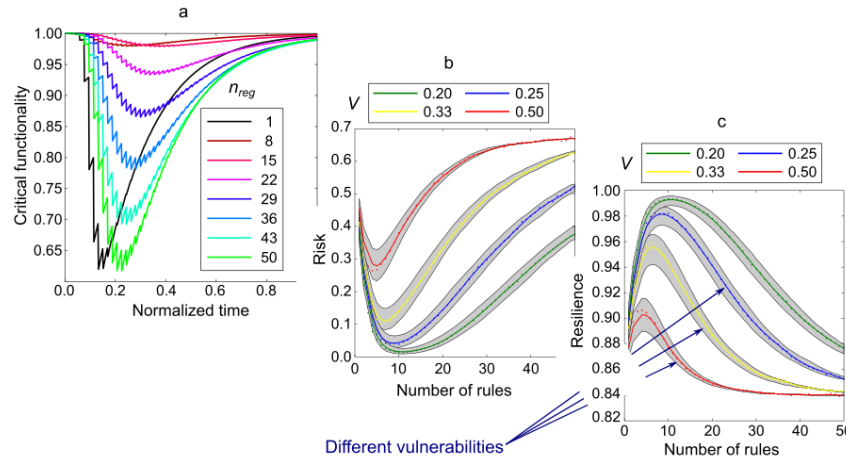


Figure 5.4: a) Critical functionality of the system as a function of time for different numbers of rules, b) risk and c) resilience as functions of rules for different vulnerability levels. The shaded areas in panels b) and c) correspond to the values of risk and resilience for threat latitudes of 4.5 and 5.5 while the lines reflect the case of $L_T = 0.5$.

incorporating behavioral science. Such a framework is needed for a number of reasons. It is in part due to the complexity of the problem and the underlying system - including data vulnerabilities, event tracking, software patching, and interdependence of stakeholders [Bauer and Van Eeten, 2009]. The need to collect and systematically utilize data from existing systems and the need to establish best practices based on goals and performance of the optimization also contribute to the necessity of the framework. Although some data and models currently exist, more is needed; not enough of the existing data are readily available and further frameworks need to be developed. The optimization would minimize the expenditure of resources on system-induced threats and focus the security resources towards cardinal threats. Research models, relating a user's ability to keep the security rules intact and the resiliency of a cyber system, are often overlooked. However, this is a key component in our cyber security eco-system and therefore in the security of critical systems and infrastructure as a whole. It is necessary to move away from reacting to threats with incremental adjustments (i.e. new rules) and move towards managing resiliency at a higher level. A select number of well-framed rules are the key to minimizing human factor risks and maximizing the resilience of cyber systems. Both over-

and under-regulating cause the system to become more vulnerable and therefore less resilient. Optimizing the regulations that increase system resilience and performance requires a systematic framework. With robust quality data and a perspective model it is possible to move towards such optimization. The results from the simple model introduced here demonstrate the hypothesized u-shaped system risk as an emergent system behavior. That fact gives us confidence that it is possible to move up the knowledge pyramid[Zeleny, 1987] toward a more explanatory model and ultimately toward a more accurate predictive model. Furthermore, it can be used to analyze more complex emergent patterns in a network to gain understanding of those patterns and how they can be controlled. The first step towards the practical application of the model developed in this study involves estimation of the minimum decision latitude (L_{\min}). This may be accomplished using cognitive psychology methods, such as testing the people's ability to follow a certain number of rules while executing certain tasks. A second step is research into a methodology to quantify the latitude employees have. The two tasks mentioned will build a base for the final stage of work which involves the development of analysis techniques to evaluate the effect of a new rule on the security of a particular system.

ACKNOWLEDGEMENTS

The text of this chapter contains reprint of the material as it appears in the publication “Resilience of Cyber Systems with Over-and Underregulation” in the Journal of Risk Analysis, 2016. Gisladdottir, V., Ganin A., Keisler J., Kepner J., Linkov I.. The dissertation author was the primary investigator and author of this article.

Chapter 6

Conclusions

We have developed a set of numerical tools to model dynamics in natural and anthropogenic networks. Fracture networks in subsurface environments provide an example of the first types of networks. The second type is represented by cyber-networks.

6.1 Heat transfer in fractured rocks

The mesh free particle method for heat transfer presented in this thesis is a general methodology, which can be used with any analytical solution that describes the physical process of transport across a single fracture embedded in an infinite matrix. We used it to simulate heat transfer in fractured media by applying it to fractal networks, which are characterized by a fracture density parameter C and fractal dimension D . Our study, reported in Chapters 2–4, leads to the following major conclusions.

- Depending on hydraulic conditions, the propagation of a cold front across fractured domains is controlled by either the fracture network or matrix block properties.
- For small fracture densities ($C = 2.5$), different values of the fractal dimension ($D = [1, 1.3]$) can lead to identical interconnected fracture networks with similar geothermal

performance.

- In fractured domains with large fracture density ($C = 6.5$) and fractal dimension ($D = 1.3$), a broad distribution of the matrix block size is obtained with the presence of small blocks that reduce the geothermal performances under slow flow conditions.
- Over a wide range of fracture densities and fractal dimensions, the heat transfer significantly deviates from the Fourier law, giving rise to anomalous effective behavior characterized by long tails.
- There is a stark contrast between the predicted performance drop of the system depending on whether one uses the Sierpinski or Watanabe fractal network.
- As fracture density increases in the fast flow hydraulic regime there is variation in the performance of the system within each network type. However it is very minimal in comparison to the performance variation between the network types.
- The heat transfer significantly deviates from the Fourier law, over a wide range of fracture densities, giving rise to anomalous effective behavior characterized by long tails.
- Computational cost is far more dependent on hydraulic regime rather than topological properties.
- Sierpinski networks although helpful in studying the fracture spacing and topography effects on different modeling parameters, it important to look at the mass flow rate when using them for reservoir performance simulation as their thermal breakthrough curves are an orders of magnitude different than Watanabe networks (representative of actual fields) for the same hydraulic regime.
- From the fractures generated for each network only the interconnected fractures, the backbone, are included in the DFN for simulation purposes. Where as the Sierpinski

networks incorporation of small fractures increases the heat sweep despite the no flow conditions and is preferable network to study the effects of fracture spacing and matrix block size on the performance of the system. The Watanabe network is more representative of the the field and better equipped for field studies.

- To compensate for the lack of realistic features in Sierpinski it would be smarter to compare equivalent flow rates or mass rates rather than hydraulic regimes which is common.
- Parameter space for which two-dimensional conduction in the matrix is of importance is identified.

6.2 Spread of viruses in cyber networks

In Chapter 5 we have an alternative application of transport in networks. Where the recptability of a cyber network to virus infiltration and propagation is dependent on the number of rules imposed on employees. Therefore requiring a limit on the number of rules impose on network members. Our study, reported in Chapter 5 leads to the following major conclusions.

- The decision latitude directly impacts the vulnerability and the resilience of the network.
- To small of a decision latitude increase the networks vulnerability.
- We identify the need for systematic data collection and appropriate metrics to enable data driven optimization of the rule base.
- While increasing the number of rules may decrease direct threats from external attacks, the excessive regulations actually increase internal vulnerabilities due to the unintentional violations of operational rules by insiders.
- The optimal number of rules necessary to regulate a cyber network efficiently is likely to be small and focused on specific critical functions that the system needs to maintain.

6.3 Future work

Although the low-computational cost of our method is attractive, improvements could be introduced in future studies. The current set up considers the matrix to be impermeable. This is representative of some reservoirs of interest (e.g. enhanced geothermal systems) but adding the flow in the matrix would widen the range of application. This can be done by leveraging the Lagrangian particle method as a component of a hybrid model, in which a continuum (Darcy-scale) representation would account for flow in the matrix. Such an extension would require an analytical solution for advection-diffusion in the matrix, which will replace the current probabilistic model. Another generalization is to improve the way we account for multi-dimensionality of heat transfer in the matrix. Our current implementation determines the entry point to the neighboring fracture to be perpendicular to the fracture of origin at a point of departure (i.e. one-dimensional spatial translation). We will expand the method to include two-dimensional spatial translation by replacing the use of first time passage with the probabilistic tools found in [?]. Finally, we will incorporate heterogeneity of matrix properties and, for example, randomly distributed fracture angles (Watanabe network) and/or heterogeneous fracture apertures (Watanabe and Sierpinski networks).

Extension of our modeling framework from two to three spatial dimensions will represent fractures as two-dimensional elements, which would enable us to study the impact of the domain and structure dimensionality by progressively improving our model. For example, representing the fractures as rectangles with a one-dimensional flow [Lee et al., 2001, e.g.] would allow us to evaluate the impact of the fracture-network dimensionality. In comparison with two-dimensional simulations, the larger number of advective paths connecting the domain borders in three dimensions should lead to a larger distribution of the advection times spent in the fractures. These fractures could also be represented as ellipses [de Dreuzy et al., 2013, e.g.] in which the heterogeneous flow velocity fields expand the distribution of advective times in

comparison with the one-dimensional flow representation. As flow velocity in the fractures impacts heat propagation in both fractures and matrix, we would also expect broader distributions of temperature of the extracted fluid with a significant anomalous behavior.

Bibliography

- Naics sectors, larger employment sizes. Technical report, US-Census Bureau, 2016.
- Shleifer A. Understanding regulation. *European Financial Management*, 2005.
- Joshua Aizenman. Financial crisis and the paradox of under- and over-regulation. Technical report, National Bureau of Economic Research, 2009.
- H. S. Al-Hadhrami and M. J. Blunt. Thermally induced wettability alteration to improve oil recovery in fractured reservoirs. *SPE Reserv. Eval. Eng.*, 4(3):179–186, 2001.
- Albert-László Barabási and Réka Albert. Emergence of scaling in random networks. *Science*, 286(5439):509–512, 1999.
- Marc Barthélemy. Spatial networks. *Physics Reports*, 2011.
- Johannes M Bauer and Michel JG Van Eeten. Cybersecurity: Stakeholder incentives, externalities, and policy options. *Telecommunications Policy*, 33(10-11):706–719, 2009.
- Brian Berkowitz and Harvey Scher. Anomalous transport in random fracture networks. *Phys. Rev. Lett.*, 79(20):4038, 1997.
- Brian Berkowitz, Curt Naumann, and Leslie Smith. Mass transfer at fracture intersections: An evaluation of mixing models. *Water Resour. Res.*, 30(6):1765–1773, 1994.
- Gudmundur S Bødvarsson and Chin Fu Tsang. Injection and thermal breakthrough in fractured geothermal reservoirs. *J. Geophys. Res. Solid Earth*, 87(B2):1031–1048, 1982.
- Geoff Boeing. Osmnx: New methods for acquiring, constructing, analyzing, and visualizing complex street networks. *Computers, Environment and Urban Systems*, 2017.
- E. Bonnet, O. Bour, N. E. Odling, P. Davy, I. Main, P. Cowie, and B. Berkowitz. Scaling of fracture systems in geological media. *Rev. Geophys.*, 39(3):347–383, 2001.
- Olivier Bour and Philippe Davy. Clustering and size distributions of fault patterns: Theory and measurements. *Geophysical Research Letters*, 26(13):2001–2004, 1999.

- D. Bruel. Impact of induced thermal stresses during circulation tests in an engineered fractured geothermal reservoir - Example of the Soultz-sous-Forets European Hot Fractured Rock Geothermal Project, Rhine Graben, France. Oil Gas Sci. Technol. - Rev. IFP, 57(5):459–470, 2002.
- Matthew Bunn. Thinking about how many guards will do the job. Risk analysis, 24(4):949–953, 2004.
- M. C. Cacas, E. Ledoux, G. de Marsily, B. Tillie, a. Barbreau, E. Durand, B. Feuga, and P. Peaudecerf. Modeling fracture flow with a stochastic discrete fracture network: calibration and validation: 1. The flow model. Water Resources Research, 26(3):479, 1990. ISSN 0043-1397.
- Jesús Carrera, Xavier Sánchez-Vila, Inmaculada Benet, Agustín Medina, Germán Galarza, and Jordi Guimerà. On matrix diffusion: formulations, solution methods and qualitative effects. Hydrogeology Journal, 6(1):178–190, 1998.
- John S Carroll. Redundancy as a design principle and an operating principle. Risk Analysis, 24(4):955–957, 2004.
- Michele Catanzaro, Marián Boguná, and Romualdo Pastor-Satorras. Generation of uncorrelated random scale-free networks. Physical Review E, 71(2):027103, 2005.
- X. Chen and P. M. Shearer. Comprehensive analysis of earthquake source spectra and swarms in the Salton Trough, California. J. Geophys. Res. Solid Earth, 116:B09309, 2011.
- V. Ciriello, M. Bottarelli, V. Di Federico, and D. M. Tartakovsky. Temperature fields induced by geothermal devices. Energy, 93(2):1896–1903, 2015.
- National Research Council et al. Disaster resilience: a national imperative, 2012.
- J. H. Cushman, M. Park, M. Moroni, N. Kleinfelter-Domelle, and D. O'Malley. A universal field equation for dispersive processes in heterogeneous media. Stoch. Environ. Res. Risk Assess., 25(1):1–10, 2011.
- Felipe P. J. de Barros, Souheil Ezzedine, and Yoram Rubin. Impact of hydrogeological data on measures of uncertainty, site characterization and environmental performance metrics. Adv. Water Resour., 36:51–63, 2012.
- J. R. De Dreuzy, Phillippe Davy, and O. Bour. Hydraulic properties of two-dimensional random fracture networks following a power law length distribution 1. Effective connectivity. Water Resources Research, 37(8):2065–2078, 2001. ISSN 00431397. doi: 10.1029/2001WR900011.
- Jean-Raynald de Dreuzy, Philippe Davy, and Olivier Bour. Hydraulic properties of two-dimensional random fracture networks following a power law length distribution: 1. Effective connectivity. Water Resour. Res., 37(8):2065–2078, 2001a.

- Jean-Raynald de Dreuzy, Philippe Davy, and Olivier Bour. Hydraulic properties of two-dimensional random fracture networks following a power law length distribution: 2. Permeability of networks based on lognormal distribution of apertures. Water Resour. Res., 37(8):2079–2095, 2001b.
- Jean-Raynald de Dreuzy, Géraldine Pichot, Baptiste Poirriez, and Jocelyne Erhel. Synthetic benchmark for modeling flow in 3D fractured media. Comput. Geosci., 50:59–71, 2013. ISSN 0098-3004.
- DOE. National renewable energy laboratory, 2015.
- Christine Doughty and Kenzi Karasaki. Flow and transport in hierarchically fractured rock. Journal of Hydrology, 263(1-4):1–22, 2002. ISSN 00221694. doi: 10.1016/S0022-1694(02)00032-X.
- B. Dverstorp, J. Andersson, and W. Nordqvist. Discrete fracture network interpretation of field tracer migration in sparsely fractured rock. Water Resour. Res., 28(9):2327–2343, 1992.
- Simon Emmanuel and Brian Berkowitz. Continuous time random walks and heat transfer in porous media. Transp. Porous Media, 67(3):413–430, 2007.
- S. Ezzedine. Impact of geological characterization uncertainties on subsurface flow using stochastic discrete fracture network models. In Annual Stanford Workshop on Geothermal Reservoir Engineering, Stanford, CA, 2010.
- W. Feller. Diffusion processes in one dimension. Transactions of the American Mathematical Society, 77(JUL):1–31, 1954.
- Alexander A Ganin, Emanuele Massaro, Alexander Gutfraind, Nicolas Steen, Jeffrey M Keisler, Alexander Kott, Rami Mangoubi, and Igor Linkov. Operational resilience: concepts, design and analysis. Scientific reports, 6:19540, 2016.
- Sebastian Geiger and Simon Emmanuel. Non-fourier thermal transport in fractured geological media. Water Resour. Res., 46(7), 2010.
- Navid Ghaffarzadegan. How a system backfires: Dynamics of redundancy problems in security. Risk analysis, 28(6):1669–1687, 2008.
- Viktoria R. Gisladottir, Delphine Roubinet, and Daniel M. Tartakovsky. Particle Methods for Heat Transfer in Fractured Media. Transport in Porous Media, 115(2):311–326, 2016.
- Neil Gunningham and Richard Johnstone. Regulating workplace safety: systems and sanctions. Oxford University Press, 1999.
- Laurence C. Hull and Karen N. Koslow. Streamline routing through fracture junctions. Water Resour. Res., 22(12):1731–1734, 1986.

- S Karra, D O'Malley, JD Hyman, HS Viswanathan, and G Srinivasan. Modeling flow and transport in fracture networks using graphs. Physical Review E, 033304(3), 2018.
- Jeremy Kepner, Vijay Gadepally, and Pete Michaleas. Percolation model of insider threats to assess the optimum number of rules. Environment Systems and Decisions, 35(4):504–510, 2015.
- O. Kolditz. Modelling flow and heat transfer in fractured rocks: dimensional effect of matrix heat diffusion. Geothermics, 24(3):421–437, 1995.
- R. Le Goc. Caractérisation et modélisation des écoulements dans les milieux fracturés. Thèse de doctorat, Université de Rennes 1, 2009a.
- Romain Le Goc. Caractérisation et modélisation des écoulements dans les milieux fracturés. PhD thesis, Université Rennes 1, 2009b.
- S H Lee, M F Lough, and C L Jensen. Hierarchical modeling of flow in naturally fractured formations with multiple length scales. Water Resources Research, 37(3):443–455, 2001.
- Igor Linkov, Todd Bridges, Felix Creutzig, Jennifer Decker, Cate Fox-Lent, Wolfgang Kröger, James H Lambert, Anders Levermann, Benoit Montreuil, Jatin Nathwani, et al. Changing the resilience paradigm. Nature Climate Change, 4(6):407, 2014.
- M. J. Lippmann and G. S. Bödavarsson. Numerical studies of the heat and mass transport in the Cerro Prieto geothermal field, Mexico. Water Resour. Res., 19(3):753–767, 1983.
- J. C. S. Long, J. S. Remer, C. R. Wilson, and P. A. Witherspoon. Porous media equivalents for networks of discontinuous fractures. Water Resour. Res., 18(3):645–658, 1982.
- Dan Lurie, Lee R Abramson, James A Vail, US Nuclear Regulatory Commission, et al. Applying statistics. Citeseer, 2011.
- Wesley A Magat, W Kip Viscusi, and Joel Huber. Consumer processing of hazard warning information. Journal of Risk and Uncertainty, 1(2):201–232, 1988.
- Ian G Main, Philip G Meredith, Peter R Sammonds, and Colin Jones. Influence of fractal flaw distributions on rock deformation in the brittle field. Geological Society, London, Special Publications, 54(1):81–96, 1990.
- Benoit B Mandelbrot. The fractal geometry of nature. Freeman, San Francisco, 1982.
- Steven J Miller. The Probability Lifesaver: All the Tools You Need to Understand Chance. Princeton University Press, 2017.
- J Molson, P Pehme, J Cherry, and B Parker. Numerical analysis of heat transport within fractured sedimentary rock: Implications for temperature probes. In Proc. Of EPA/NGWA Fractured Rock Conference: State of the Science and Measuring Success in Remediation, pages 24–26, 2007.

- Framework for Improving Critical Infrastructure Cybersecurity. National Institute of Standards and Technology, 41 edition, 2014.
- Ivars Neretnieks. A note on fracture flow dispersion mechanisms in the ground. Water Resources Research, 19(2):364, 1983. ISSN 0043-1397.
- Shlomo P. Neuman. Trends, prospects and challenges in quantifying flow and transport through fractured rocks. Hydrogeol. J., 13(1):124–147, 2005.
- Shlomo P. Neuman and Daniel M. Tartakovsky. Perspective on theories of non-Fickian transport in heterogeneous media. Adv. Water Resour., 32(5):670–680, 2009.
- A. Wille Nordqvist, Y W Tsang, C F Tsang, Bjorn Dverstorp, and Johan Andersson. A variable aperture fracture network model for flow and transport in fractured rocks. Water Resour. Res., 28(6):1703–1713, 1992.
- S. Painter and V. Cvetkovic. Upscaling discrete fracture network simulations: An alternative to continuum transport models. Water Resour. Res., 41(2), 2005. doi: 10.1029/2004WR003682.
- Scott Painter, Vladimir Cvetkovic, James Mancillas, and Osvaldo Pensado. Time domain particle tracking methods for simulating transport with retention and first-order transformation. Water Resour. Res., 44(1), 2008. doi: 10.1029/2007WR005944.
- K. Pruess, C. Oldenburg, and G. Moridis. Tough2 user’s guide version 2. Lawrence Berkeley National Laboratory, 1999.
- Delphine Roubinet, Jean-Raynald de Dreuzy, and Philippe Davy. Connectivity-consistent mapping method for 2-D discrete fracture networks. Water Resour. Res., 46(7):W07532, 2010a.
- Delphine Roubinet, Hui-Hai Liu, and Jean-Raynald de Dreuzy. A new particle-tracking approach to simulating transport in heterogeneous fractured porous media. Water Resour. Res., 46(11), 2010b.
- Delphine Roubinet, J.-R. de Dreuzy, and Daniel M. Tartakovsky. Semi-analytical solutions for solute transport and exchange in fractured porous media. Water Resour. Res., 48(1):W01542, 2012.
- Delphine Roubinet, Jean-Raynald de Dreuzy, and Daniel M. Tartakovsky. Particle-tracking simulations of anomalous transport in hierarchically fractured rocks. Computers & Geosciences, 50:52–58, jan 2013a.
- Delphine Roubinet, Jean-Raynald de Dreuzy, and Daniel M. Tartakovsky. Particle-tracking simulations of anomalous transport in hierarchically fractured rocks. Computers & Geosciences, 50:52–58, jan 2013b.

- Ankur Roy, Edmund Perfect, William M. Dunne, and Larry D. McKay. Fractal characterization of fracture networks: An improved box-counting technique. Journal of Geophysical Research: Solid Earth, 112(12):1–9, 2007. ISSN 21699356. doi: 10.1029/2006JB004582.
- A. Ruiz Martinez, D. Roubinet, and D. M. Tartakovsky. Analytical models of heat conduction in fractured rocks. J. Geophys. Res. Solid Earth, 119(1):83–98, 2014.
- M. Saar. Review: Geothermal heat as a tracer of large-scale groundwater flow and as a means to determine permeability fields. Hydrogeol. J., 19(1):31–52, 2011.
- Scott D Sagan. The problem of redundancy problem: why more nuclear security forces may produce less nuclear security. Risk analysis, 24(4):935–946, 2004.
- M Sahimi. Flow Phenomena in Rocks - from Continuum Models to Fractals, Percolation, Cellular-Automata, and Simulated Annealing. Reviews of Modern Physics, 65(4):1393–1534, 1993. ISSN 0034-6861. doi: 10.1103/RevModPhys.65.1393.
- Harvey Scher, Gennady Margolin, and Brian Berkowitz. Towards a unified framework for anomalous transport in heterogeneous media. Chem. Phys., 284(1-2):349–359, 2002.
- CH Scholz, NH Dawers, J-Z Yu, MH Anders, and PA Cowie. Fault growth and fault scaling laws: preliminary results. J. Geophys. Res. Solid Earth, 98(B12):21951–21961, 1993.
- Mischa Schwartz and Thomas Stern. Routing techniques used in computer communication networks. IEEE Transactions on Communications, 28(4):539–552, 1980.
- Adam Sedgewick. Framework for improving critical infrastructure cybersecurity, version 1.0. Technical report, 2014.
- Andrei Shleifer. Understanding regulation. European Financial Management, 11(4):439–451, 2005.
- Brij Bhusan Saran Singhal and Ravi P Gupta. Applied hydrogeology of fractured rocks. Springer Science & Business Media, 2010.
- H. Stehfest. Algorithm 368: Numerical inversion of laplace transform. Communication of the ACM, 13(1):47–49, 1970.
- E. A. Sudicky and E. O. Frind. Contaminant transport in fractured porous media: Analytical solutions for a system of parallel fractures. Water Resour. Res., 18(6):1634–1642, 1982. doi: 10.1029/WR018i006p01634.
- Anna Suzuki, Yuichi Niibori, Sergei a. Fomin, Vladimir a. Chugunov, and Toshiyuki Hashida. Analysis of Water Injection in Fractured Reservoirs Using a Fractional-Derivative-Based Mass and Heat Transfer Model. Mathematical Geosciences, 47(1):31–49, 2015.
- D. H. Tang, E. O. Frind, and E. A. Sudicky. Contaminant transport in fractured porous media: Analytical solution for a single fracture. Water Resour. Res., 17(3):555–564, 1981.

- George A Truskey, Fan Yuan, and David F Katz. Transport phenomena in biological systems. Pearson/Prentice Hall Upper Saddle River NJ, 2004.
- Donald L Turcotte. Fractals and chaos in geology and geophysics. Cambridge university press, 1997.
- USGPO. Code of Federal Regulations (Annual Edition). U.S. Government PUblishing Office, 2015.
- Valentin Wagner, Tao Li, Peter Bayer, Carsten Leven, Peter Dietrich, and Philipp Blum. Thermal tracer testing in a sedimentary aquifer: field experiment (Lauswiesen, Germany) and numerical simulation. Hydrogeol. J., 22(1):175–187, 2014.
- M Mitchell Waldrop. How to hack the hackers: The human side of cybercrime. Nature, 533 (7602), 2016.
- J. S. Y. Wang, C. F. Tsang, N. G. W. Cook, and P. A. Witherspoon. A study of regional temperature and thermohydrologic effects of an underground repository for nuclear wastes in hard rock. J. Geophys. Res. Solid Earth, 86(B5):3759–3770, 1981. ISSN 2156-2202.
- K. Watanabe and H. Takahashi. Fractal Geometry Characterization of geomthermal reservoir fracture networks. Journal of Geophysical Research: . . ., 100:521–528, 1995.
- Shaw-Yang Yang and Hund-Der Yeh. Modeling heat extraction from hot dry rock in a multi-well system. Appl. Therm. Eng., 29(8-9):1676–1681, 2009.
- Milan Zeleny. Management support systems: Towards integrated knowledge management. Human systems management, 7(1):59–70, 1987.
- Quanyan Zhu and Tamer Başar. Robust and resilient control design for cyber-physical systems with an application to power systems. In Decision and Control and European Control Conference (CDC-ECC), 2011 50th IEEE Conference on, pages 4066–4071. IEEE, 2011.